TECHNISCHE UNIVERSITÄT WIEN

Herstellung und Charakterisierung von Mid-IR Semiconductor Loaded Plasmonischen Wellenleitern für die chemische Sensorik

ausgeführt zum Zwecke der Erlangung des akademischen Grades eines Diplom-Ingenieurs

im Rahmen des Studiums Materialwissenschaften

eingereicht von

BSc. Ismail Cem Doganlar
Matrikelnummer 11736194

an der Fakultät für Elektrotechnik und Informationstechnik

der Technischen Universität Wien

Betreuung: Univ. Prof. Dr. Gottfried Strasser
Co-Betreuung: Projektass Dr. Borislav Hinkov

Wien, 21. Oktober 2022

Ismail Cem Doganlar	Gottfried Strasser

TECHNISCHE UNIVERSITÄT WIEN

Fabrication and characterization of mid-IR semiconductor loaded plasmonic waveguides for chemical sensing

submitted in partial fulfillment of the requirements for the degree of Masters

in

Materials Sciences

by

BSc. Ismail Cem Doganlar
Registration Number 11736194

to the Faculty of Electrical Engineering and Information Technology

at the TU Wien

Supervisor: Univ. Prof. Dr. Gottfried Strasser
Co-Supervisor: Projektass Dr. Borislav Hinkov

Vienna, 21st October, 2022

Ismail Cem Doganlar	Gottfried Strasser

Erklärung zur Verfassung der Arbeit

BSc. Ismail Cem Doganlar

Hiermit erkläre ich, dass ich diese Arbeit selbständig verfasst habe, dass ich die verwendeten Quellen und Hilfsmittel vollständig angegeben habe und dass ich die Stellen der Arbeit – einschließlich Tabellen, Karten und Abbildungen –, die anderen Werken oder dem Internet im Wortlaut oder dem Sinn nach entnommen sind, auf jeden Fall unter Angabe der Quelle als Entlehnung kenntlich gemacht habe.

Wien, 21. Oktober 2022

Ismail Cem Doganlar

Abstract

Mid-infrared spectroscopy offers an effective solution to identify absorption lines of target molecules, e.g. in liquid environment. This is due to the fundamental absorptions lines of many molecules lie in this wavelength range. Unfortunately, still most equipment used for such experiments is rather bulky, significantly hampering real-time measurements in liquids so far. Reducing the size of bulky photonic components is one possible way to tackle this problem, but it is a challenging task to realize chip-scale devices. Mid-infrared plasmonic structures can be a solution to that, since they can confine the light to the wavelength-scale, e.g. when using metal-dielectric structures. Those structures can be used in different types of liquid samples, but need protection in aggressive solutions. Despite a large number of papers published in the field, a promising material concept against degradation in the liquid with low optical losses is still missing.

In this thesis work, broadband Ge-based plasmonic waveguide structures suitable for liquid spectroscopy are studied when combining them with different protective surface films. First, state-of-the-art Ge/Au-based SPP waveguides are fabricated. Based on the material configuration and the nature of SPPs when using thin Ge confinement layers, the main portion of the mode (>96%) propagates in the surrounding medium (e.g. the liquid sample). This results in relatively long propagation lengths. Combined with the simplicity of the device fabrication procedure, it makes Ge-based waveguides a very promising liquid sensing platform in the mid-infrared spectral range. The optical losses and coupling efficiency of the coated waveguides are extracted by applying an effective cut-back technique. This demonstrates, that the Ge-based material system outperforms existing plasmonic waveguides in the same wavelength range, with its optical losses lower than 15 dB/mm at 9.38 μm.

In total four different nanometer-thick insulation layers were used for protection in this work, including: Al_2O_3, ZrO_2, TiO_2 and HfO_2. They were deposited by Atomic Layer Deposition (ALD). The modal characteristics and propagation losses of the coatings are compared. In addition, both coated and uncoated devices, are submerged into DI-H_2O for testing their protective capabilities. This is based on the fact, that water etches bare Ge-surfaces. After 90 min of water exposure, the surface quality of the thin oxide films is investigated by Scanning Electron Microscope (SEM) and Atomic Force Microscope (AFM). The optical losses of coated and uncoated devices are compared to demonstrate the suitability of this approach scheme for broadband spectroscopy in aqueous solution.

Kurzfassung

Die Spektroskopie im mittleren Infrarot bietet eine effektive Lösung zur Identifizierung der Absorptionslinien von Zielmolekülen, z.B. in flüssiger Phase. Dies ist darauf zurückzuführen, dass die grundlegenden Absorptionslinien vieler Moleküle in diesem Wellenlängenbereich liegen. Leider sind die meisten Geräte, für für solche Experimente ziemlich sperrig, was Echtzeitmessungen in Flüssigkeiten erheblich erschwert. Die Verringerung der Größe sperriger photonischer Komponenten ist jedoch eine anspruchsvolle Aufgabe speziell um Sensoren auf Chipgröße zu realisieren. Plasmonische Strukturen in mittleren Infrarot können das Licht auf die Sub-Wellenlängen-Skala für metall-dielektrische Strukturen beschränken. Diese Strukturen können in verschiedenen Arten von flüssigen Phasen verwendet werden,müssen aber in aggressiven Flüssigkeiten geschützt werden. Trotz einer großen Zahl von Arbeiten auf diesem Gebiet, fehlt es noch immer an einem vielversprechenden Materialkonzept gegen Degradation in der Flüssigkeit mit geringen optischen Verlusten.

In dieser Arbeit, wurden breitbandige plasmonische Wellenleiterstrukturen auf Ge-Basis untersucht, die sich für die Flüssigkeitsspektroskopie eignen, besonders wenn sie mit verschiedenen schützenden Oberflächenschichten kombiniert werden. Zunächst werden die hochmodernen Ge/Au-basierten surface plasmon polariton (SPP) Wellenleiter hergestellt. Dank der Materialkonfiguration und der Art der SPPs befindet sich der größte Teil der Mode (>96%) in der Luft. Dies führt zu relativ großen Propagationslängen. In Kombination mit dem einfachen Herstellungsverfahren und der relativ großen Propagationslänge bieten Ge-basierte Wellenleiter die gewünschte Plattform für die Sensorik im mittleren Infrarotbereich. Die optischen Verluste und die Kopplungseffizienz der Wellenleiter werden durch Anwendung einer ëffektiven cut back techniqueëxtrahiert. Das Ge-basierte Materialkonzept übertrifft bestehende plasmonische Wellenleiter durch niedrige optische Verluste von weniger als 15 dB/mm bei 9.38 μm Wellenlänge.

Zum Schutz wurden vier verschiedene nanometer dicke Isolationsschichten verwendet darunter Al_2O_3, ZrO_2, TiO_2 und HfO_2. Sie wurden durch Atomic Layer Deposition (ALD) aufgebracht. Die modalen Eigenschaften sowie die Ausbreitungsverluste der Beschichtungen wurden verglichen. Darüber hinaus wurden sowohl beschichtete als auch unbeschichtete Proben in DI-H_2O getaucht, um die Resilienz bzw. Schutzwirkung der Isolationsschichten zu testen. Dies beruht auf der Tatsache, dass Wasser offene Ge-Oberflächen angreift. Nach 90 Minuten im Wasser wurde die Oberflächenqualität der

dünnen Oxidschichten mit dem Rasterelektronenmikroskop Mikroskop (SEM) und Rasterkraftmikroskop (AFM) untersucht. Die optischen Verluste von beschichteten und unbeschichteten Bauteilen wurden verglichen, um die Eignung dieses Konzepts für breitbandige Flüssigkeitsspektroskopie in wässriger Lösung zu demonstrieren.

Acknowledgements

Throughout the course of my work, I would have not succeeded without the assistance and encouragement of numerous people. I sincerely acknowledge and thank everyone who has in some way helped my personal, academic and professional development.

Foremost, I would like to express my special thanks of gratitude to Prof. Gottfried Strasser for giving me this opportunity to conduct my research in his group. His vision and immense knowledge in the field, when combined with a good sense of humor makes him a true mentor.

My greatest acknowledgement to my co-supervisor Dr. Borislav Hinkov. He has been supportive and has given me the freedom to pursue my own ideas. His friendship, insightful discussion and suggestions on various research topics helped me to grow as a research scientist.

I would like to extend my appreciation to the fellow group members for their assistance. In particular, Mauro David, for close collaboration to my research and his contribution to simulations in this work. Elena Arigliani and Niklas Brandacher, for sharing and discussing many valueble ideas on their research output. Georg Marschick, Anna Lardschneider and Dominik Koukola, for their friendship and all the great times we shared together. I want to thank Dr. Masiar Sistani and Dr. Daniele Nazzari for their contribution to surface characterization of the waveguides and sharing their expertise on oxide films. To Dr. Hermann Detz for his contribution to the ellipsometry measurements of oxide films. To Werner Schrenk for his advises and to Andreas Linzer for his technical assistance. For all the events and the good times, I would like to thank Stefania Isceri, Florian Pilat, Mikołaj Piotrowski, Miriam Giparakis, Dr. Nikola Opačak, Dr. Hedwig Knötig, Dr. Rolf Szedlak, Sandro Dal Cin, Maximilian Beiser, Andreas Windischofer, Prof. Benedikt Schwarz and Prof. Aaron Maxwell Andrews.

Lastly, I am deeply grateful for tremendous amount of support of my family, both spiritual and physical. My parents, Emine and Ferruh, thanks to your guidance and your faith in me without any doubt, I was able to push this far. My precious brother, Alp, you have been always my best friend and surely the most important person to make me think creatively. Of course I cannot end this without thanking Mişa -our lovely cat- her existence was a huge source of motivation, even we are miles away separated from each other.

Contents

CHAPTER 1

Introduction

The mid-infrared spectral region has attracted a lot of attention for chemical spectroscopy, as the fundamental absorption lines of several molecules lie in this range. In chemical sensing the wavelength region from 2 to 15 μm is especially important, since it allows for high selectivity [1]. The mid-infrared spectral range therefore enables applications in various areas including chemical sensing, microbiological diagnosis, optical communication and security [2].

Although, mid-infrared spectroscopic sensing has a long history, with decades of development on instruments, there is still plenty of space for research in optimizing the material selection of those sensors [3]. In this sense germanium is attractive as material of choice because it is highly transparent throughout the mid-infrared spectral range [4]. It therefore extends the usable wavelength range to covering almost the whole long wave infrared spectrum, which allows the fabrication and development of new mid-infrared photonic devices [5] (see Fig. 1.1).

As an example, germanium-gold plasmonic ridge waveguides combined with microliter-fluidic concept can be used to detect molecules in aqueous solution [[7], [8]], exploting the surface sensitive characteristics of this configuration. On the other hand in liquid environments, low loss and non-degradable waveguide structures are needed to efficiently address liquid sensing including protein solutions or solvents like isopropyl alcohol, which is the objective of this project (see Fig. 1.2).

In this study we investigated the impact of additional nanometer thick high quality protective surface films deposited by atomic layer deposition (ALD), on parameters like waveguide losses for the plasmonic mode and the robustness of the waveguide structure towards exposure to water which typically etches Ge over time. We analyze low loss high-k dielectrics including long wave mid-infrared oxide materials including Al_2O_3, ZrO_2, TiO_2 and HfO_2 for their (long wave) mid-infrared losses and robustness.

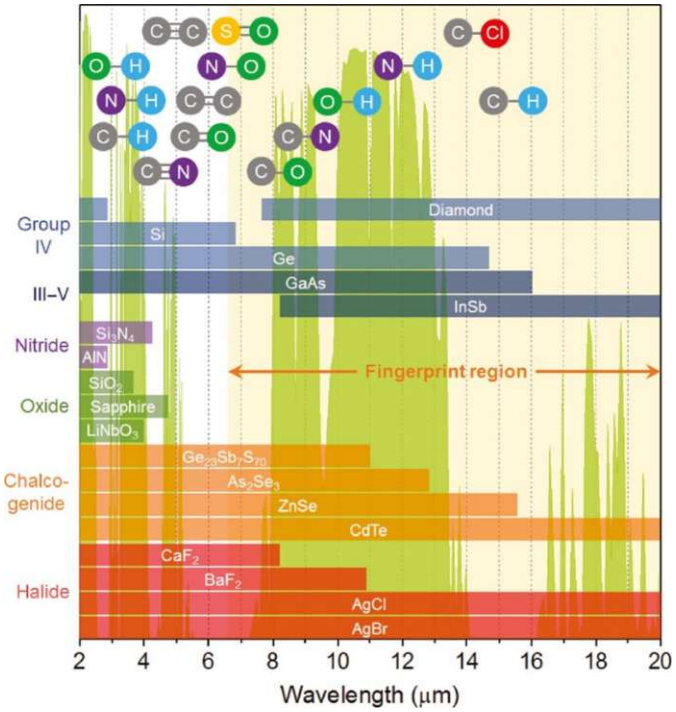

Figure 1.1: Absorption spectra from a variety of organic molecules and the used materials in the mid-infrared region. Taken from [6].

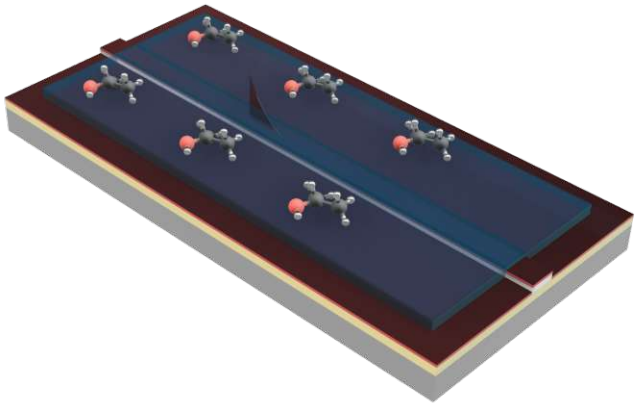

Figure 1.2: Sketch of insulated (for surface protection) germanium-gold plasmonic waveguide with isopropyl alcohol molecues on top.

1.0.1 Thesis Outline

The present thesis consists of four main parts. The first part is dedicated to the theoretical description of surface plasmons and more importantly surface plasmon polaritons. The second part is devoted to modelling and simulation of insulated-germanium based waveguides. The third part is characterization of optical losses of the waveguides and liquid experiment and finally the last one reviews the investigation of surface topography and optical losses of both coated and uncoated waveguides. Below, a brief explanation of the content of each chapter is presented.

Chapter 2 | Fundamentals

In this chapter, we provide the comprehensive theoretical background to understand this thesis. First, we begin with an overview of surface plasmons and we introduce three classical examples of coupling between photons and electronic plasma. Then, we explain the propagation length of the surface plasmon polaritons and different configurations to excite them. Furthermore, we introduce the semiconductor loaded surface plasmon polariton waveguide concept, where we replaced the dielectric layer with a semiconductor. We show why this concept is superior to the other material systems shown in literature at the wavelength of interest (9.38 μm). Finally, we provide a simple procedure for fabrication of insulated-germanium based SPP waveguides. Hereby, waveguides will be insulated with four different oxide films, including Al_2O_3, ZrO_2, TiO_2 and HfO_2.

Chapter 3 | Waveguide Modelling and Simulations

This chapter is devoted to defining the ideal geometrical parameters of the semiconductor loaded SPP waveguides, in order to obtain a good trade off between transmission losses and mode confinement. This is done by a FEM based numerical tool via using the complex refractive index values of each individual layer from ellipsometry. In the last part of this chapter, a comparative study will be made between several oxide films to show their impact on the modal characteristics and the propagation length.

Chapter 4 | Experimental Procedures

In this chapter, we demonstrate an optical setup to characterize the fabricated waveguides. The cut-back technique is performed to extract the optical losses and coupling efficiency of the waveguides. In the next part of this chapter, we will investigate material behavior of the thin-oxide films under water exposure.

Chapter 5 | Results

In this last chapter, we will analyze the protective capabilities of coatings. We provide surface topography characterization results from Scanning Electron Microscope (SEM) and Atomic Force Microscope (AFM). In addition, optical losses of both coated and uncoated waveguides will be presented to propose the most promising low loss plasmonic material system for liquid sensing.

CHAPTER 2

Fundamentals

2.0.1 Surface Plasmons

In the last decades, the impact of optic and photonic components on our daily lives increased remarkably. This includes areas like optical communication for information technologies and optical sensing for health and security concerns. However, conventional photonic systems are limited by the diffraction limit at subwavelength scale, to manipulate the light [9]. This problem can be overcome, when photons are coupled to subwavelength-scale structures by nano- and micro-structuring of metals [[10], [11], [12]]. The resonant interaction between the surface charge oscillation and the electromagnetic field of the light gives surface plasmons its unique properties. This could eventually lead to miniaturized photonic circuits and solves fundamental problems in sensing [13] and on-chip communications [14].

The interaction of photons and the free electron gas inside the conductive materials can be described by the Drude approach, often referred to as plasma model. The motion of the free electron with angular frequency ω in the plasma can be described as:

$$m\frac{\partial^2 x}{\partial t^2} + m\gamma\frac{\partial x}{\partial t} = e\ exp(-i\omega t) \tag{2.1}$$

Under the assumption of the deflection of electrons from their equilibrium position it can be written as $x(t) = A\ exp(-i\omega t)$, the amplitude of the electron's oscillation is given by

$$A = -\frac{e}{m}\frac{1}{\omega^2 + i\gamma\omega} \tag{2.2}$$

After that, the polarization can be calculated as $P = enx = \epsilon_0 \chi E$, where n is the density of the free electron gas, ϵ_0 the permittivity of free space and χ the polarizability. This leads us to the description of the relative permittivity of the plasmonic material (ϵ_m) given as

$$\epsilon_m = \epsilon_b + \chi = \epsilon_b - \frac{\omega_p^2}{\omega(\omega + i\gamma)} \tag{2.3}$$

with the so called plasma frequency

$$\omega_p^2 = \frac{\epsilon^2 n}{\epsilon_0 m} \tag{2.4}$$

where γ the scattering rate for electrons in the metal and ϵ_b the material's background permittivity. Herein, the plasma frequency is mainly determined by the concentration of the free charge carriers inside the medium. In noble metals, the electron concentration is fixed ($n \sim 10^{22}\ cm^{-3}$), but in semiconductor structures, the plasma frequency can be tuned (e.g. by doping or substitution of metal with materials like nitrides/oxides) to near-infrared, mid-infrared and THz frequency ranges [[15], [16], [17]].

Finally, we can split the complex dielectric function into the real and imaginary components via using the relation of the damping rate and the relaxation time as $\gamma = 1/\tau$ [18] as

$$\epsilon_1 = \epsilon_0 \left(1 - \frac{\omega_p^2 \tau^2}{1 + \omega^2 \tau^2}\right) \tag{2.5}$$

$$\epsilon_2 = \epsilon_0 \left(\frac{\omega_p^2 \tau^2}{\omega(1 + \omega^2 \tau^2)}\right) \tag{2.6}$$

In the regime of very low frequencies, where $\omega\tau \ll 1$, the imaginary component becomes dominant $\epsilon_2 \gg \epsilon_1$. Here, metals are mainly absorbing with an absorption coefficient of

$$\alpha = \left(\frac{2\omega_p^2 \tau \omega}{c^2}\right)^{1/2} \tag{2.7}$$

The Beer's law of absorption also applies to the decrease of the electric field inside the metal as $exp(-z/\delta)$, where δ is the skin depth

$$\delta = \sqrt{\frac{2}{\alpha_o \omega \mu_o}} \tag{2.8}$$

In the regime of high frequencies, $1 < \omega\tau < \omega_p\tau$, the imaginary part of the complex refractive index becomes non dominant and metals retain their metallic character.

In the free electron model, $\omega \gg \omega_p$ leads to $\epsilon \to 1$. For the noble metals (e.g. Au, Ag, Cu) extension of this model is needed in this frequency regime, since the field is induced by interband transitions.

$$\epsilon = \epsilon_0 \left(\epsilon_{r,\infty} - \frac{\omega_p^2}{\omega^2 + j\gamma\omega} \right) \tag{2.9}$$

We introduce in the following sections three classical examples of coupling between photons and electronic plasma:

- localized surface plasmon (LSP) resonances in metallic nanostructures
- spoof SPP modes
- surface plasmon polariton (SPP) waves at metal/dielectric interface

2.0.2 Localized Surface Plasmons

Localized surface plasmons are non-propagating excitations of charge density oscillations of metallic nanostructures coupled to the electromagnetic field. For demonstration (see Fig. 2.1), let's assume that we have a spherical metallic nanoparticle with diameter a, embedded in a dielectric medium of ϵ_d and excited by an electromagnetic wave (of amplitude E_o). Since the particle is smaller than the incident wavelength, the electromagnetic field distribution of the particle can be solved by the quasistatic approximation [19] as

$$E_{in} = \frac{3\epsilon_d E_o}{\epsilon_m + 2\epsilon_d} \tag{2.10}$$

Hereby, the induced field inside the metallic sphere is strongly enhanced when $\epsilon_m \to -2\epsilon_d$. This field enhancement is limited by absorption inside the metallic particle and frequency detuning from resonant condition [9]. This phenomena can be used for example in solar cells [20]. Metal nanopartices are also ideal for optical sensing platforms [[21], [22]], since the resonant frequency has a strong dependency on the dielectric medium. Furthermore, combining with the good biocompatibility and well-developed surface chemistry, gold nano particles can be used in applications like cellular imaging as well [23].

At mid-infrared frequencies, where $|\epsilon_m| \to \infty$, the field inside the metal nanoparticle becomes really small, so that the properties of noble metals resemble those of perfect conductors. This prevents such localized surface plasmon excitations from being supported by subwavelength metallic particles. Therefore, in mid-infrared highly-doped semiconductors are used to mimic the visible-photonics of noble metals.

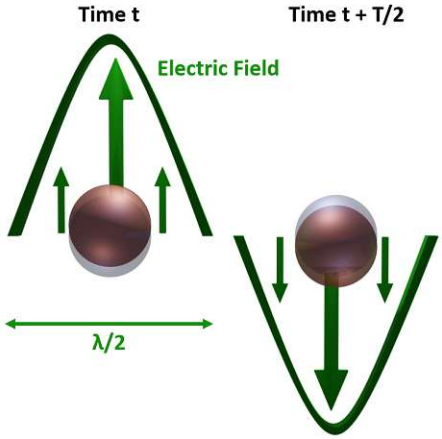

Figure 2.1: Schematic of localized surface plasmon polaritons. The blue and red spheres represent the electron cloud and the metal respectively.

2.0.3 Spoof Plasmons

In the mid-infrared, SPPs are poorly confined at the metal/dielectric interface and are therefore difficult to control using plasmonic structures. However, the behavior of SPPs can be mimicked in this frequency range via structuring the surface by periodic features [24]. These are so called spoof plasmons and thanks to their design flexibility they can be used in a wide range of wavelengths. An example of such a structure is shown in Fig. 2.2. Williams et. al. showed by perforating a planar copper surface with square arrays [25]. These plasma like response could have a number of applications including for highly sensitive biological sensing [26] in optical communication [27] or optical focus/imaging [28].

When the surface of the structure under the considerations is a metal, each array acts as a waveguide (subwavelength) with the core (of permittivity ϵ_h and permeability μ_h) [9]. Therefore, the field inside the array can be defined as a linear combination of the waveguide modes. The contribution from the fundamental mode becomes dominant, when the distance between the arrays a is smaller than the wavelength of interest, as $a \ll \lambda_0$. Here, we can desribe the collective response of the multiple arrays by the effective medium theory.

$$\omega_{pl}^2 = \frac{\pi c}{\epsilon_h \mu_h} \tag{2.11}$$

This yields the plasma-like response with the effective plasma frequency [25]. For the finite conductive noble metals, correction of this theory becomes important especially for the mid-infrared frequency range [29].

In the next section, we will describe the main working principle of our plasmonic waveguide design. This will be further detailed in the following sections (2.0.4 and 2.0.5).

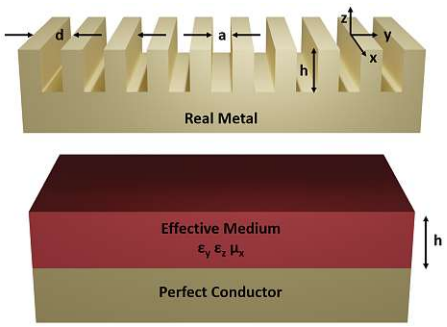

Figure 2.2: Schematic of spoof plasmons based metal structure with subwavelength grooves. Here, the grooves have a width of a, depth h, and periodicity d. This can be approximated by the effective medium theory with the parameters ϵ_y, ϵ_z and μ_x. Adapted from [9].

2.0.4 Surface Plasmon Polaritons

Surface Plasmon Polaritons (SPPs) are interactions between light and electrons in a bulk metal or heavily doped semiconductor [18]. The excited surface electromagnetic modes propagate at the interface between a material with positive real part of the permittivity (ϵ_1) and a negative real part of the permittivity (ϵ_2), as can be seen in the Fig. 2.3. The positive sign of the dielectric function holds for the dielectric and negative sign of the dielectric function holds for metals in most cases.

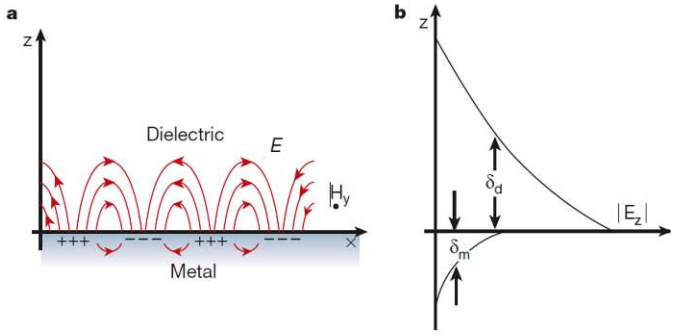

Figure 2.3: (a) Representative sketch of a surface plasmon polariton propagation on a planar metal/dielectric interface in x-direction (z=0). (b) The decay length of the field in the dielectric medium is represented by δ_d and in the metal by δ_m. Taken from [10].

SPP waves are evanescently confined in perpendicular direction, which offers new possibilities for applications in sensing and optical communications in the mid-infrared region [30] [31].

The wave equation can be solved by "Maxwell Equations" and results in two optical modes namely, transverse magnetic mode (TM) and transverse electric mode (TE). The related solution to the wave equation in a medium is described as follow [32]:

$$\nabla \cdot \mathbf{D} = \rho_{ext} \tag{2.12}$$

$$\nabla \cdot \mathbf{B} = 0 \tag{2.13}$$

$$\nabla \cdot \mathbf{E} = -\frac{\partial \mathbf{B}}{\partial t} \tag{2.14}$$

$$\nabla \cdot \mathbf{H} = \mathbf{J_{ext}} + \frac{\partial \mathbf{D}}{\partial t} \tag{2.15}$$

where $\mathbf{H}$ is the magnetic field, $\mathbf{E}$ is the electric field, $\mathbf{D}$ is the dielectric displacement vector and $\mathbf{B}$ is the magnetic induction or magnetic flux density. Since these 4 macroscopic fields are linked via polarization (electric dipole moment per unit volume), we could further derive the equation with given ϵ_0 (vacuum permittivity), ϵ (permittivity) and μ_0 (magnetic permeability) as:

$$\mathbf{D} = \epsilon_0 \epsilon \mathbf{E} \tag{2.16}$$

$$\mathbf{B} = \mu_0 \mathbf{H} \tag{2.17}$$

Combining the curl equations (2.14)-(2.15) leads to:

$$\nabla \times \nabla \times E = -\mu_0 \frac{\partial^2 \mathbf{D}}{\partial t^2} \tag{2.18}$$

Using the identities $\nabla \times \nabla \times \mathbf{E} \equiv \nabla(\nabla \cdot \mathbf{E}) - \nabla^2 \mathbf{E}$ and $\nabla \cdot (\epsilon \mathbf{E}) \equiv \mathbf{E} \cdot \nabla \epsilon + \epsilon \nabla \cdot \mathbf{E}$ can be written as:

$$\nabla(-\frac{1}{\epsilon}\mathbf{E} \cdot \nabla \epsilon) - \nabla^2 \mathbf{E} = -\mu_0 \epsilon_0 \epsilon \frac{\partial^2 \mathbf{E}}{\partial t^2} \tag{2.19}$$

For the negligible variation of the dielectric profile on the order of wavelength, the previous expression can be further simplified to the wave equation for the electric field:

$$\nabla^2\mathbf{E} - \frac{\epsilon}{c^2}\frac{\partial^2\mathbf{E}}{\partial t^2} = 0 \tag{2.20}$$

Assuming a harmonic time dependence $\mathbf{E}(\mathbf{r},t) = \mathbf{E}(\mathbf{r})e^{-iwt}$ of the electric field yields the Helmholtz equation as:

$$\nabla^2\mathbf{E} + k_0^2\epsilon\mathbf{E} = 0 \tag{2.21}$$

where $k_o = \frac{\omega}{c}$ is the wave vector propagating in the x-direction at z = 0 (see Fig. 2.3). Hereby, the propagating wave can be described as $\mathbf{E}(x,y,z) = \mathbf{E}(z)e^{i\beta x}$, with complex parameter $\beta = k_x$, which is called the propagation constant. It corresponds to the component of the wave vector in the direction of propagation. Inserting this into the previous expression (2.21) yields a wave equation of the form

$$\frac{\partial^2\mathbf{E}(z)}{\partial z^2} + (k_0^2\epsilon - \beta^2)\mathbf{E} = 0 \tag{2.22}$$

Here, a similar equation is valid for the magnetic field **H**. Using the curl equations (2.14, 2.15) and harmonic time dependence, we arrive to the following set of coupled equations

$$\frac{\partial E_y}{\partial z} = -i\omega\mu_0 H_x \tag{2.23}$$

$$\frac{\partial E_x}{\partial z} - i\beta E_z = i\omega\mu_0 H_y \tag{2.24}$$

$$i\beta E_y = i\omega\mu_o H_z \tag{2.25}$$

$$\frac{\partial H_y}{\partial z} = i\omega\epsilon_0\epsilon E_x \tag{2.26}$$

$$\frac{\partial H_x}{\partial z} - i\beta H_z = -i\omega\epsilon_0\epsilon E_y \tag{2.27}$$

$$i\beta H_y = -i\omega\epsilon_0\epsilon E_z \tag{2.28}$$

This system allows two sets of self-consistent solutions with different polarization properties of the propagating waves which are:

- Transverse magnetic (TM) mode with the field components E_x, E_z and H_y are nonzero,
- Transverse electric (TE) mode with components H_z, H_z and E_y.

For TM modes, the system equation is reduced to:

$$E_x = -i\frac{1}{\omega\epsilon_0\epsilon}\frac{\partial H_y}{\partial z} \tag{2.29}$$

$$E_z = -\frac{\beta}{\omega\epsilon_0\epsilon}H_y \tag{2.30}$$

and the wave equation of TM mode is:

$$\frac{\partial^2 H_y}{\partial z^2} + (k_0^2\epsilon - \beta^2)H_y = 0 \tag{2.31}$$

Using the equation set (2.29, 2.30 and 2.31) yields the solutions:

$$H_y(z) = A_2 e^{i\beta x}e^{-k_{z,2}z} \tag{2.32}$$

$$E_x(z) = iA_2\frac{1}{\omega\epsilon_0\epsilon_2}k_{z,2}\, e^{i\beta x}e^{-k_{z,2}z} \tag{2.33}$$

$$E_z(z) = -A_1\frac{\beta}{\omega\epsilon_0\epsilon_2}e^{i\beta x}e^{-k_{z,2}z} \tag{2.34}$$

For the condition z>0:

$$H_y(z) = A_1 e^{i\beta x}e^{k_{z,1}z} \tag{2.35}$$

$$E_x(z) = -iA_1\frac{1}{\omega\epsilon_0\epsilon_1}k_{z,1}\, e^{i\beta x}e^{k_{z,1}z} \tag{2.36}$$

$$E_z(z) = -A_1\frac{\beta}{\omega\epsilon_0\epsilon_1}e^{i\beta x}e^{k_{z,1}z} \tag{2.37}$$

For the condition z<0, $k_{z,i}$ (i = 1, 2) component of the wave vector is perpendicular to the interface in both media and decay length into the metal, δ_m (corresponds to the absorption in the metal), determined by skin depth (see Fig. 2.3b) [10]. The continuity of H_y and $\epsilon_i E_z$ needs to be satisfied by $A_1 = A_2$ at the interface:

$$\frac{k_{z,2}}{k_{z,1}} = -\frac{\epsilon_2}{\epsilon_1} \tag{2.38}$$

One of the required conditions to confine light at the interface demands that the materials to have opposite sign of the real part of their permittivities, i.e a metal/doped

semiconductor and an insulator.The wave equation needs to be fulfilled with H_y, which yields:

$$k_{z,1}^2 = \beta^2 - k_0^2\epsilon_1 \tag{2.39}$$
$$k_{z,2}^2 = \beta^2 - k_0^2\epsilon_2 \tag{2.40}$$

From the last equations we come to the dispersion relation for SPP propagating in interface between two medias as:

$$\beta = k_0\sqrt{\frac{\epsilon_1\epsilon_2}{\epsilon_1 + \epsilon_2}} \tag{2.41}$$

This expression is valid for both real and complex ϵ_1 for conductors with and without attenuation. Furthermore, continuity of E_y and H_x leads to the condition $A_1(k_1 + k_2) = 0$ at metal/dielectric interface and it reveals that no surface modes exist for TE polarization. Therefore, surface plasmon polaritons only exist for TM polarization.

The Propagation Length of the SPPs

In large vectors and higher frequencies, damping of the conduction electron oscillation in ideal conductors is neglected ($lim[\epsilon_1(\omega)] = 0$) and it reaches the limit condition at frequency value ω_{sp}, which is called "the characteristic plasma frequency:

$$\omega_{sp} = \frac{\omega_p}{\sqrt{1 + \epsilon_2}} \tag{2.42}$$

However, the mode at this frequency suffer from both free-electron and interband damping. Therefore, the propagation constant, β, is a complex number, which describes mode's effective wavelength and attenuation as the mode propagates [33]. The propagation length can be described with attenuation as:

$$L_{SPP} = \frac{1}{2Im\{\beta\}} \tag{2.43}$$

The propagation constant is mainly denoted as the ohmic losses by metal. This remains still as a challenging problem for plasmonic applications, but can be optimized by choosing the right waveguide geometry. In the next sections we will discuss in more detail about it with giving the proposed waveguide structures related to that.

Excitation of Surface Plasmon Polaritons

Confinement of the surface plasmon modes can be achieved when propagation constant β is bigger than the wave vector k [18], but to couple light on metal/dielectric interface phase mismatch needs to be overcome. In literature different techniques have been proposed to solve this problem including excitation by charged particles, prism coupling, grating coupling and near-field coupling.

The excitation of surface plasmon polaritons is achieved firstly by [Ritchie,1957] via using electron diffraction at metal films. In principal, the excitation mechanism works as fast electrons with high energy ($\approx$ 50 keV) penetrate through the film and transfer their momentum on unstructured metal surfaces, which was shown using low energy electrons in studies of [Vincent and Silcox, 1973, Pettit et al., 1975] for surface excitation [34].

Besides exciting surface plasmon polaritons by electrons, it has been demonstrated that using prism to couple light with the principle mechanism of attenuated total internal reflection is also conveniently possible. This way the wave vector of light can be increased via high refractive index prism, which enables exciting SPPs at the metal/dielectric interface. In literature there are two fundamental configurations given for prism coupling: Otto [35] and Kretschmann- Raether Configuration [36].

In Otto Configuration the metal surface is separated from prism by a dielectric spacing (a thin dielectric layer or air). Once the incident angle becomes larger than the critical angle of total internal reflection, tunneling occurs on the boundary between dielectric and metal.

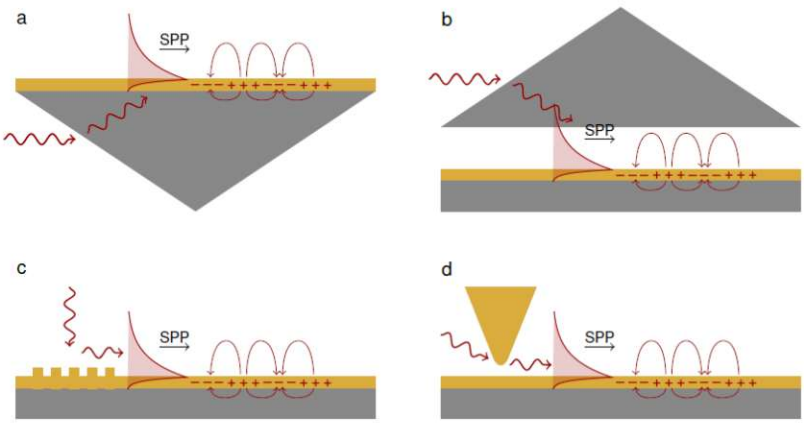

Figure 2.4: Different configurations to excite SPPs from free space including a) Kretschmann-Raether Configuration b) Otto Configuration c) Grating Coupling and d) near-field coupling. Taken from [5].

On the other hand in Kretschmann Configuration a thin metal is deposited on the bottom side of the prism and the SPP excitation occurs through the total reflected light

wave of the evanescenct field as shown in the Fig. 2.4.

Another optical technique is named as “grating coupling”, which overcomes the phase mismatch via patterning a nano-fabricated structure on top of the metal surface. A simple representation of such a structure is given in Fig. 2.5.

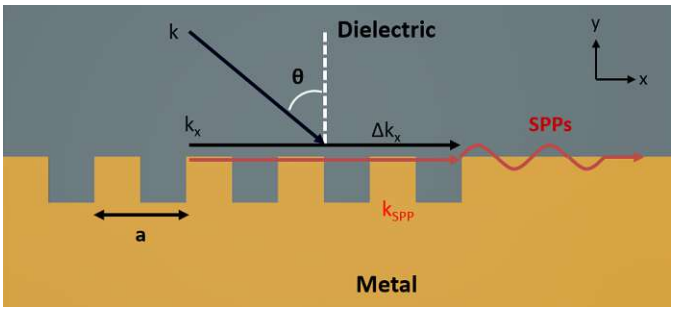

Figure 2.5: Grating couplers to provide phase matching of the free space wave and in plane wave vectors.

Correlated relation between the incident wave vector k, grating vector g, the lattice constant of the grating a and propagation constant β is given as:

$$\beta = ksin\theta \pm vg \tag{2.44}$$

The equation is fulfilled, where $g = \frac{2\pi}{a}$ and v = 1, 2, 3 .... The reverse process can also take place to out-couple SPPs propagating from the surface, which results in the decrease of the in-plane momentum and radiation of the light.

One last method can be given as “near-field excitation”, which relies on local excitation of SPPs with the help of a small probe tip. The light is confined to a spot on a metal surface with a diameter much smaller than the the wavelength of the corresponding SPPs. Furthermore, the positioning capability of this method allows excitation of SPPs at different locations, which can be seen seen in Fig. 2.4 and 2.6 [37].

2.0.5 Semiconductor Loaded Surface Plasmon Polariton Waveguides

In strong contrast to simple metal layers used for VIS/near-infrared plasmonics, other concepts are needed in the mid-infrared for efficient mode confinement and guiding along the metal-dielectric interface [38]. Semiconductor Loaded Surface Plasmon Polariton Waveguides (SLSPPWs) provide strong lateral confinement due to the increased permittivity arising from the additional dielectric material at the surface which positively impacts SPP. Dielectric loaded surface plasmon polariton waveguides (DLSPPWs) can be used in the telecom wavelengths [39], since they lead an increased SPP propagation length, as well as compressing the SPPs by an order of magnitude in mid-infrared [40]. Moreover, thanks

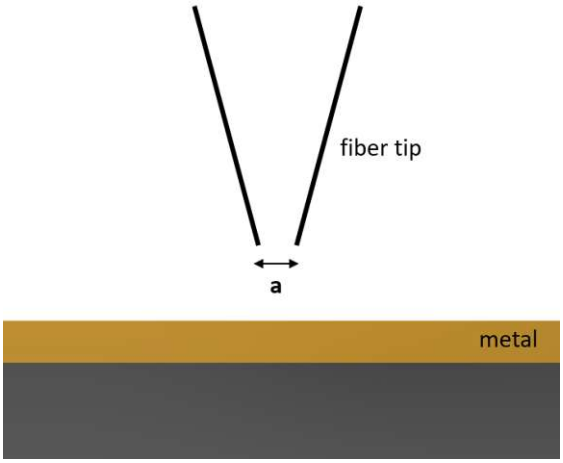

Figure 2.6: Local Excitation of SPPs using near field illumination.

to their fabrication simplicity and tuning capabilities of optical properties, DLSPPWs are the ideal candidates for on-chip devices.

Depending on the geometry (height and the width) of the dielectric ridge, propagation length and mode effective index can be adjusted. The additional dielectric layer thickness results in an increase of the effective mode index, which significantly confines the mode in vertical direction. Besides, with using relatively thin Ge (e.g. $\sim$ 200 nm at 6.1 μm wavelength) on top of the gold, most of the optical mode (>95%) still resides in the surrounding medium, which is quite favorable for spectroscopic measurements. Moreover, a thin dielectric layer typically has a long SPP propagation length, since the mode is typically confined to the scale of the used wavelength [41]. Furthermore, another advantage of DLSPPWs apart from support of the optical mode properties is, its geometry allows carrying of electrical signals. Combining both photonics and electronics on the same platform opens advanced applications as plasmonic devices including Mach-Zehnder Interferometers (MZIs) for interfering plasmons [[42], [43]], waveguide ring resonators [[44], [45], [46]] and directional couplers (DCs) [[47]] (see Fig. 2.7). The mode effective index, mode confinement and propagation length of the designed waveguides will be discussed in the Chapter 3-Waveguide Modelling and Simulations more in more detail.

In this thesis, the term "Semiconductor Loaded Surface Plasmon Waveguides" refers to the replacement of the more often used dielectric layer with a semiconductor layer. The resulting SLSPPWs can have advantages in thermal behavior (if the semiconductor has a better thermal conductivity as the compared dielectric) and low-loss capabilities in the mid-infrared spectral range when choosing materials like the spectrally very broadband Ge. For that reason, investigation of the semiconductor layer is needed to fulfill certain conceptual requirements i.e., a suitable refractive index n and low extinction coefficient. In literature, there are several examples given as dielectric layers for the wavelength of interest including SiN, SiO_x, Al_2O_3, which can not be used in such configurations regarding their high losses. Chalcogenides and halides are also suggested, but difficulties

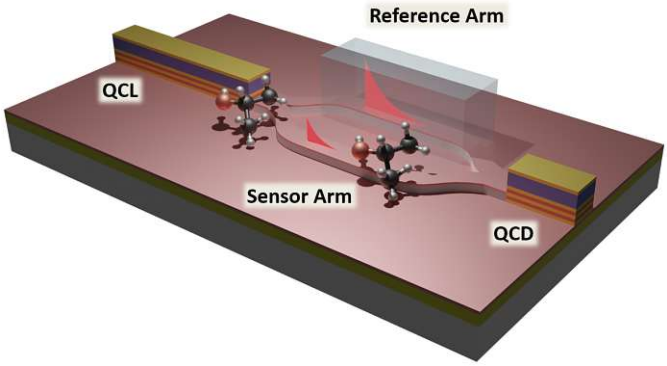

Figure 2.7: Schematic of one of the future monolithic/hybrid on-chip QCLD based MZIs (Ge-based semiconductor loaded surface plasmon polariton waveguide in the middle).

of their processing (toxic materials) make them a not ideal choice as well. Similarly, germanides and silicates require high-annealing temperatures with material integration compatibility problems to the monolithic on-chip approach. As it is discussed in the earlier chapter germanium on other hand, is a good candidate with suitable complex refractive index properties in the part of the mid-infrared spectral range of interest, which makes it the chosen semiconductor material in this study. We will show in the following section, fabrication of such Ge-based SLSPPWs with respect to their geometrical influence on both propagation length and mode effective index.

2.0.6 Fabrication Steps

Fabrication of the Ge-based SLSPPWs is conducted at the TU Wien internal cleanroom facilities Center for Micro- and Nano-Structures (ZMNS), using state-of-the-art semiconductor fabrication techniques. The overall processes can be divided into the four main steps namely, sputtering, lithography, liftoff and atomic layer deposition (ALD) (see Fig. 2.8). In the following chapters we will explain each step individually with respect to their fundamental working principles and finally, fabrication of Ge-based SLSPPWs will be described.

Sputtering

Sputtering and evaporation processes have been widely used in the deposition of thin films in recent decades. In contrast to evaporation, sputtering involves not thermal, instead physical vaporazation of solid atoms from a surface by bombardment with typically Ar-plasma [48].

Sputter deposition depends on:

- Good vacuum using energetic argon ions (less than 10^{-5} Torr : base pressure)

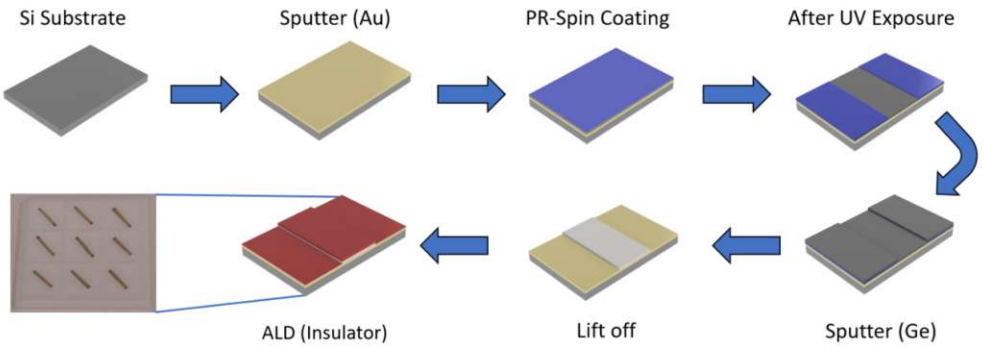

Figure 2.8: Fabrication steps of Ge-based SLSPPWs including passivation of the devices by ALD. In last step, samples are cleaved to different lengths (1.0, 1.5 and 2 mm) to apply the cut-back technique for measuring the coupling losses.

- A low pressure gas environment (<5 mTorr : working pressure) to prevent gas phase collisions of transported particles from the target material, via using the plasma as the source of ions
- A higher gas pressure in the regime, where gas phase collisions and "thermalization" of the ejected particles occur but pressure is low enough that gas phase nucleation can be neglected (pressure greater than 5 mTorr, less than 50 mTorr)

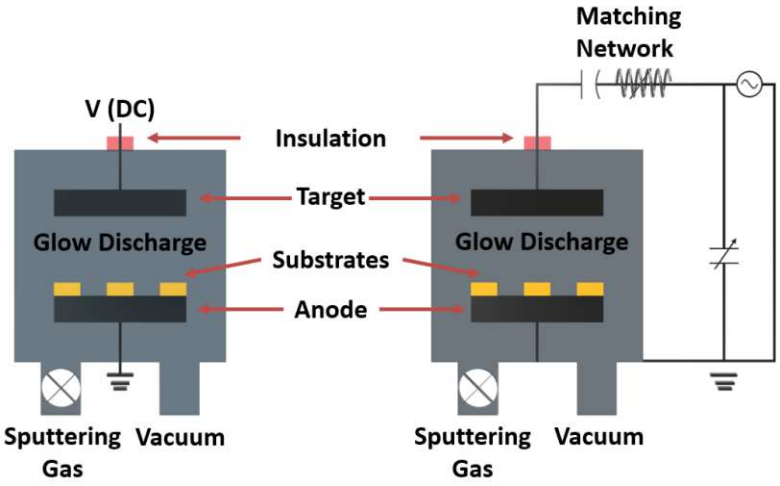

Figure 2.9: Schematics of the DC (left) and RF (right) sputtering systems. Taken and modified from [49].

The deposition process takes place in a vacuum chamber filled with chemically inert gas for sputtering, such as Ar to create compounds, N_2 and O_2 for oxides/nitrides, as illustrated in Fig. 2.9.

DC sputtering, RF sputtering, and magnetron sputtering are the three most common

sputtering process configurations. Each uses a different energy source to accelerate the ions for sputtering.

Lithography

The desired waveguide patterns are transferred on the sputtered metal surface using optical lithography, which requires applying a light-sensitive material called photoresist on the sample. There are two photoresist namely, positive and negative resist.

Fabrications of integrated chips typically start with cleaning and, if necessary, cleaving of the substrate (Si <100> substrates in our case). As for the cleaning, there are several methods given including, cleaning the wafer with solvents like acetone and isopropyl alcohol or alternatively in an oxygen plasma or in case in an ultrasonic bath. In case of sputtered samples, further cleaning procedures are not needed. Next step to ensure the adhesion between photoresist and sample surface , is the use of an adhesion promoter such as hexamethyldisilazane (HDMS) or Ti-prime. Photoresist is applied to the wafer at rotation speeds ranging from 1000 to 5000 rpm. Depending on the desired pattern, the sample is treated with rather positive or negative photoresist. Then, the sample is baked on a hot plate to improve adhesion and remove the solvent from the photoresist, which follows by mask alignment and exposure [50].

A photo mask is used to transfer patterns onto the surface of the wafer. Alignment marks on the mask help the positioning of the wafer to be exposed. After that, the mask is brought in contact with the resist on the wafer surface. As next step, the photoresist is exposed by ultraviolet light. In positive photoresist light exposed areas are washed with the developer. On the other hand, in negative photoresist only exposed areas on the surface remain as can be seen below in Fig. 2.10 (d).

Liftoff

Instead of using etching processes (e.g. chemical etching or dry etching plasma systems), removal of the photoresist material is performed with liftoff procedure. The lift-off process strongly depends on the extent of side wall angle of the resist profile.

Compared to the etching methods liftoff does not require further cleaning methods. But on the other hand, during metal-liftoff some defects including, rough metal edge, unlifted metal or bent metal lines can occur, hereby additional cleaning treatments can be needed [51].

Fabrication of Ge-based Semiconductor Loaded Surface Plasmon Polariton Waveguides

The fabrication of SLSPP waveguides started with cleaving silicon carrier wafers (2-inch size, 275 μm thick) into 1 cm x 1 cm samples. The cleaving is performed on <100> direction with respect to the crystal orientation of silicon substrate. Then, the sample is cleaned in ultrasonic bath. To prevent adhesion problems of the gold, we sputtered

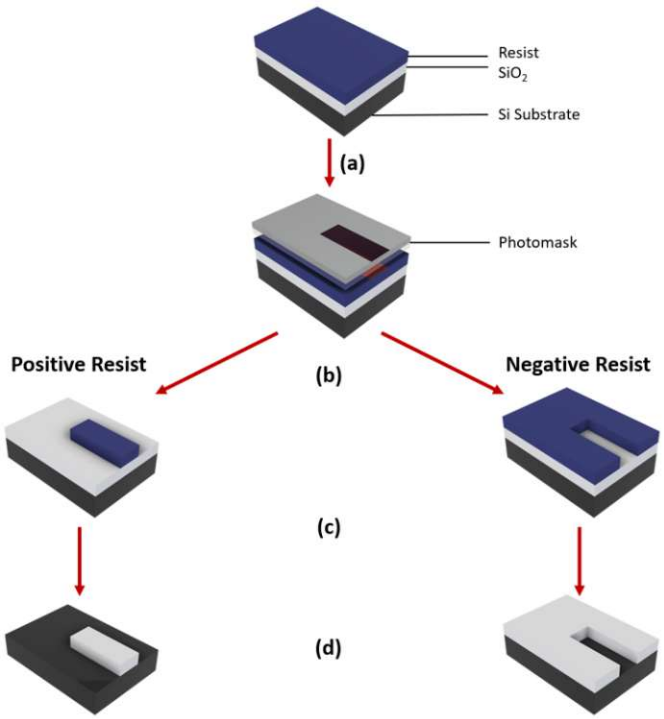

Figure 2.10: (a) Photomask (illustrated as dark grey) is used to transfer the pattern on the sample, (b) The application of positive and negative photo resist on SiO_2 pattern, (c)-(d) Exposure and development steps of pholithography.

10 nm of TiO_2 (see Table 2.1) onto the surface as adhesion promoter before the sputter of the gold layer. 100 nm of gold in 7 cycles is sputtered with a deposition rate of 0.55 nm/s (see Table 2.2).

Power	50 W
Work Pressure	8.10^{-3}mbar
Cycles	3 x 30 s
Ar	8.10^{-3}mbar

Table 2.1: Sputtering deposition rates of TiO_2.

Power	25 W
Work Pressure	8.10^{-3}mbar
Cycles	7 x 30 s
Ar	8.10^{-3}mbar

Table 2.2: Sputtering deposition rates of Au.

Here, layer quality of deposition is important as the roughness and not uniformed

Power	25 W
Work Pressure	8.10^{-3}mbar
Cycles	12 x 60 s
Ar	8.10^{-3}mbar

Table 2.3: Sputtering deposition rates of Ge.

Table 2.4: Process parameters of sputtering deposition of (Table 2.1) 10 nm TiO_2, (Table 2.2) 100 nm Au, (Table 2.3) 300 nm Ge. The sample is placed on a holder and loaded into the sputtering chamber of the Ardenne LS 320 S sputter system. Deposition of thin films are conducted under the high Ar-pressures (8.10^{-3}mbar) and process steps are monitored.

coating results in additional scattering losses of the plasmonic mode propagating along the interface. Thus far, we mentioned sputtering as chosen physical deposition method because of its simplicity and fast applicability. But also evaporation could be an alternative method to deposite gold with a lower roughness (if needed). In our work we actually did not see an improvement when using evaporated gold instead of the sputtered one. In fact we even saw higher resulting waveguide losses possibly due to a higher background doping in the Au layer.

The desired waveguide pattern is achieved by a standard optical lithography. The sample is first treated with Ti-prime adhesion promoter to prevent any possible adhesion problems between photoresist and metal surface as mentioned before. Then, image reversal process is applied as choosing AZ5214E photoresist to spin coat on gold sputtered sample. Accelerated rotation speed is chosen to firstly covering the substrate with the resist, which followed by uniformly spreading it with given parameters as listed below in Table 2.5. Here again, the photoresist layer has quite some importance, since any possible dirt of particles on the sample can be transferred into the structure on the sample after exposure.

Photoresist	AZ5214E
Spin Coating	4000 rpm – acceleration 2000 rpm – 35 s
Soft Baking	1 min at 100°C
Exposure	15 s (edge removal)
Development	AZ351B:H_2O (1:4) – 40 s + Rinse: 60 s
Exposure	0.7 s for mesa
Bake	1 min at 120°C
Flood Exposure	15 s (without mask)
Development	AZ351B:H_2O (1:4) – 22 s + Rinse: 60 s

Table 2.5: Lithograpy parameters for SLSPP waveguide fabrication.

Before the mask alignment step, sample is placed on a hot plate and held for 1 min at 100°C for removing the solvent. Then, the photomask is cleaned with acetone and

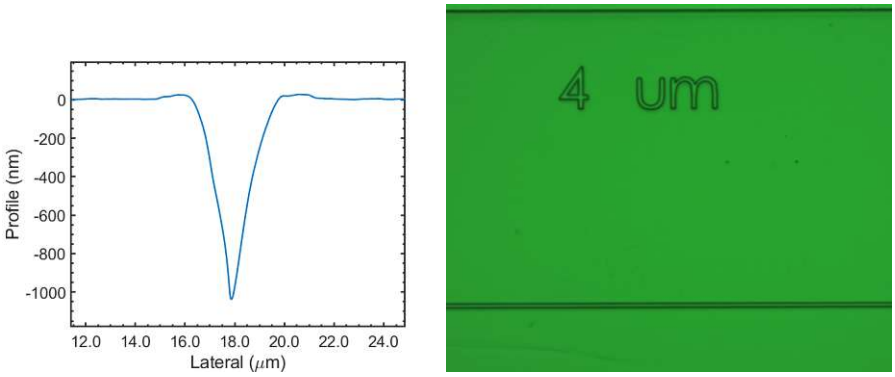

(a) (b)

Figure 2.11: After the development step wall profiles (a) and microscopic image of the corresponding 4 µm width waveguide ridge with x 8 magnification (b). The image reversal process gives a negative wall profile, which is ideal for applying lift-off.

isopropyl alcohol to prevent transferring any possible contamination on substrate. The mask alignment is done via mask aligner SÜSS MicroTec MJB-4. As next step, sample is exposed under the photomask via aligning to respective markers on mask and making soft contact with the mask. Immediately after exposure, sample needs to be submerged into chemical solvent (developer) to remove photoresist. In image reversal process, sample is exposed under UV light in 2 cycles for both structures (mesa) and edges, therefore there are 2 development steps involved. After each individual development step sample is rinsed in distilled water and dried with N_2 gun.

In lithography, development, baking and exposure times needs to be adjusted to obtain good resist profiles. Fig. 2.11. represents the profile of resist and related microscopic image after development step.

Once development step is completed, 300 nm germanium is deposited on sample with sputtering process as indicated in Table 2.3. As described in the last Section (2.0.6), instead of etching liftoff procedures is performed for such waveguides to remove the resist. This is conducted by typically placing sample into a glass holder filled with acetone and putting it on hot-plate for 1 h at $40°C$. However, in some cases where this is not strong enough to remove all of the photoresist, unwanted metal parts or even some rough edges can be observed on patterned structure. This requires an additional treatment including one of the options, which is listed below.

- applying liftoff with longer times
- splashing acetone on sample
- placing sample into ultrasonic bath (10% power, 10 -15 s)

The fabricated Ge-based SLSPP waveguides of height 300 nm and width 9 μm, is confirmed measuring by “DekTak Profilometer” left-center-right positions of those samples

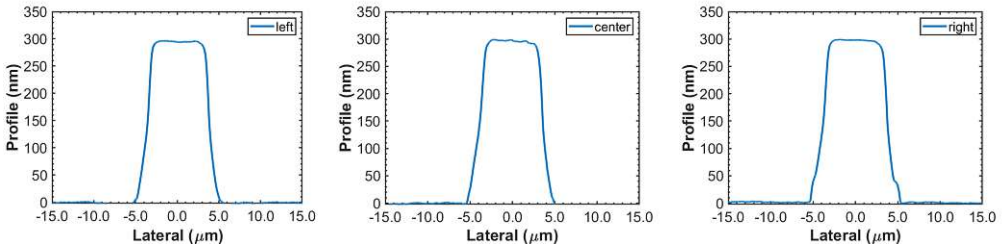

(a) (b) (c)

Figure 2.12: Ge based – semiconductor loaded waveguide profiles taken from respectively (a) left - (b) center- (c) right sides.

(see Fig. 2.12). Hence, we show that there are no significant additional losses caused by waveguide profiles, since height of ridges are not varying along the sample and their optical images in Fig. 2.13. Asymmetrical profiles can result in degradation of optical constants, considering the volume of the dielectric layer depends on it.

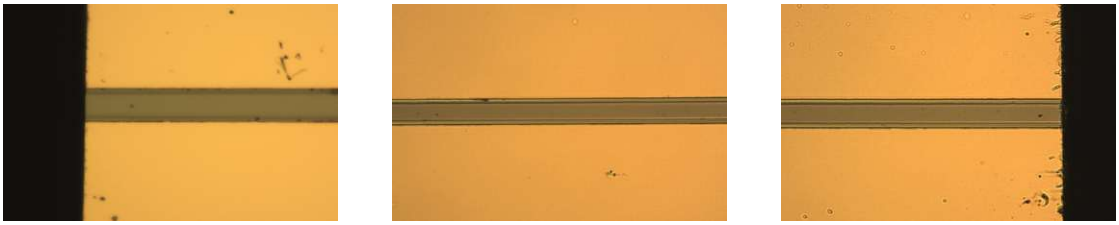

Figure 2.13: Microscopic images of fabricated Ge based SLSPP waveguides (x50 magnification). The images are taken from left, center and right position along the Ge ridge to demonstrate the homogeneity along the waveguide structure.

As last step, samples are cleaved into 1.0, 1.5 and 2.0 mm long waveguides to apply the so called "cut-back technique" later, which will be described in detail in Chapter 4. The initiated scribing length is defined as 10 - 15% of the waveguide length (JFP Microtech, S-100 Scriber Breaker). Hereby, using a scribing machine allows us to precisely control distribution of the initiated load and therefore, we can avoid additional lateral cracks on the surface of the sample. However, some exceptions might occur during cleaving due to defects from fabrication steps as its outlined in Fig. 2.14. This can be resulted in non -straight facets and needs to be optimized to prevent additional coupling losses on the end product.

Atomic Layer Deposition(ALD)

Atomic layer deposition is a vapor-phase thin-film deposition method for deposition of variety of materials. The material growth process depends on self-limiting surface reactions. As result it offers high conformality, thickness control of films and tunable material composition. As a consequence of these characteristics ALD is used widely in

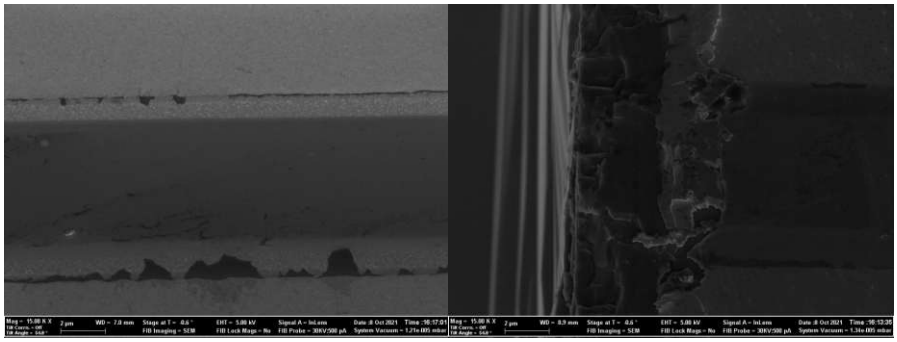

(a) (b)

Figure 2.14: (a) Ge-based SLSPP waveguide profile. Some residuals from lift-off can be seen near the waveguide section. (b) Left facet image of waveguide after cleaving. Out-coupling facet indicates non-straight profile, which adds additional coupling losses during optical characterization of the device. (both images are taken by scanning electron microscope).

microelectronics industry and many other research applications [52].

A typical ALD process consists of sequential use of gaseous chemical precursors (reactants). The reactions occur between precursors and substrate in a vacuum chamber (<1 Torr), leaves no more than one mono-layer on the substrate. It is followed by the removal of the excess of precursor molecules by purging of the reaction chamber with an inert gas (N_2 or Ar). As next, counter reactant precursor pulse and purge steps take place to obtain one layer of the desired material. Desired film thickness can be achieved by adjusting the number of process cycles. An illustration for the process steps is given Fig. 2.15.

Generally, ALD process temperature is chosen below a certain temperature. The reason behind it is controlling the competition between chemisorption and physical adsorption to work in the regime, where chemisorption becomes the dominant driving of the process. This temperature is called “temperature window” and with the chemisorption phenomenon makes ALD a self-limited process. As a consequence, only a mono-layer can be absorbed at the surface at the time independent from pressure and substrate changes [53].

In fabrication of Ge-based SLSPPWs, we used ALD process to deposit 10 nm thick insulator layers of Al_2O_3, ZrO_2, TiO_2 and HfO_2 for future studies such as chemical sensing in liquid environment. Roughness of those waveguide surfaces are characterized by atomic force microscopy (AFM). Additional optical losses caused by depositing such oxide films will be discussed at the Chapter 5 in detail.

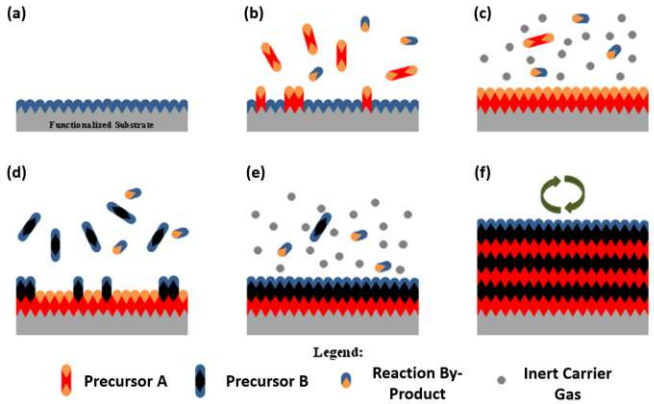

Figure 2.15: Representative process flow chart of ALD a) functionalization of the substrate surface (b) precursor A is interacting with the surface (c) purging/evacuation of the excess precursor (d) precursor B is given to the reaction chamber (e) second purging step (f) repeated process cycles until the desired thickness of the coating material is achieved. Image is taken from [52].

CHAPTER 3

Waveguide Modelling and Simulations

Waveguide Geometry

Waveguides are the structures used to propagate optical modes efficiently over certain distances. Their geometry can be differed with material choice or operating wavelength of light. The well-known dielectric waveguides have an optical "core" (high refractive index material) surrounded by a low index material called the "cladding" as structure for mode guiding [54].

The material system of waveguides used in this thesis consists of four different insulator layers including Al_2O_3, ZrO_2, TiO_2 or HfO_2 on top of un-doped germanium stripe as we discussed in Chapter 2. As plasmonic metal layer, Au is used, which is on top of the Si substrate (a 10 nm TiO_2 thin layer is used as adhesion layer between the Au and the Si substrate). The whole geometry is presented in Fig. 3.1.

The geometrical parameters are chosen via numerical simulations in a way that a good trade off between transmission losses and mode confinement is obtained and therefore, chemical sensing applications can be addressed. As result, a rectangular shaped semiconductor-loaded plasmonic waveguide scheme is used as a favorable waveguide architecture for fabrication of waveguides at operating wavelength $\lambda = 9.38$ μm. In this configuration each Ge-stripe has a width of 9 μm and height of 300 nm, together with lengths of 1.0, 1.5 and 2.0 mm, respectively. The waveguides are insulated with the above mentioned 10 nm thick oxide films to prevent degradation against liquids, which results in additional attenuation as can be seen in Fig. 3.4.

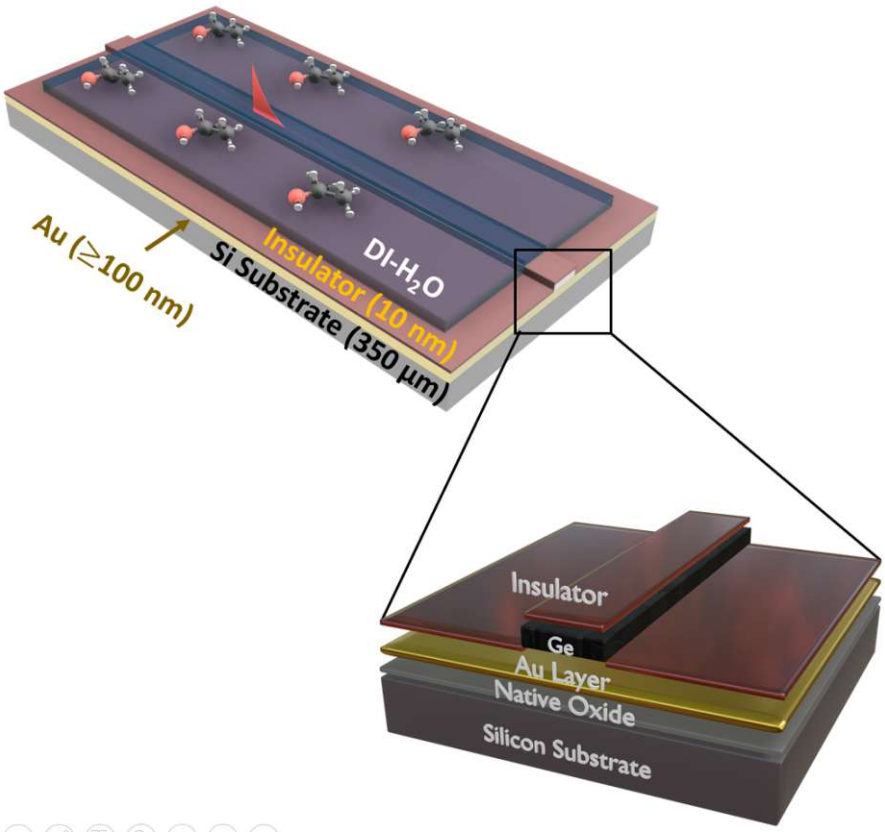

Figure 3.1: Schematic representation of insulated Ge-based plasmonic waveguides when submerged into DI-H_2O. The layer thickness of Si substrate, gold and insulator is given. Inset: cross-sectional view of each individual layer is presented.

Optical Mode Area

We studied the optical mode area for the waveguide geometry described in the previous section. Here, the complex refractive index of the multi-layers is individually characterized using ellipsometry and the modal area simulations below were obtained using FEM-based commercial software COMSOL (v5.5). The modal characteristics are extracted by the propagation constant, which is defined as $\gamma = \alpha + j\beta = -\lambda$, where α is its attenuation constant, β is propagation constant and λ is the eigenvalue returned by the solver [55]. The propagation length is calculated as mentioned in Section 2.0.4:

$$L_p = \frac{1}{2Im\beta} \tag{3.1}$$

defined as the distance where its mode power reduced by factor of 1/e. The imaginary part of the propagation length (or α) corresponds to attenuation, and it is described in

logarithmic dB scale as:

$$\alpha_{dB/m} = 20\alpha \log e \tag{3.2}$$

The effective mode area A_{eff} is defined as the ratio of total mode energy and peak energy density. It can be obtained from the equation:

$$A_{eff} = \frac{1}{Max\{W(\mathbf{r})\}} \int_{A^{\infty}} W(\mathbf{r}) dA \tag{3.3}$$

Lastly, the energy density W(r), at position r is expressed with [33]:

$$W(\mathbf{r}) = \frac{1}{2} Re \left\{ \frac{d[\omega\epsilon(\mathbf{r})]}{d\omega} \right\} |\mathbf{E}(\mathbf{r})|^2 + \frac{1}{2}\mu_0 |\mathbf{H}(\mathbf{r})|^2 \tag{3.4}$$

where ϵ is permittivity, μ_0 is permeability, $\mathbf{E}(\mathbf{r})$ is the electric field and $\mathbf{H}(\mathbf{r})$ is the magnetic field component of the respective mode.

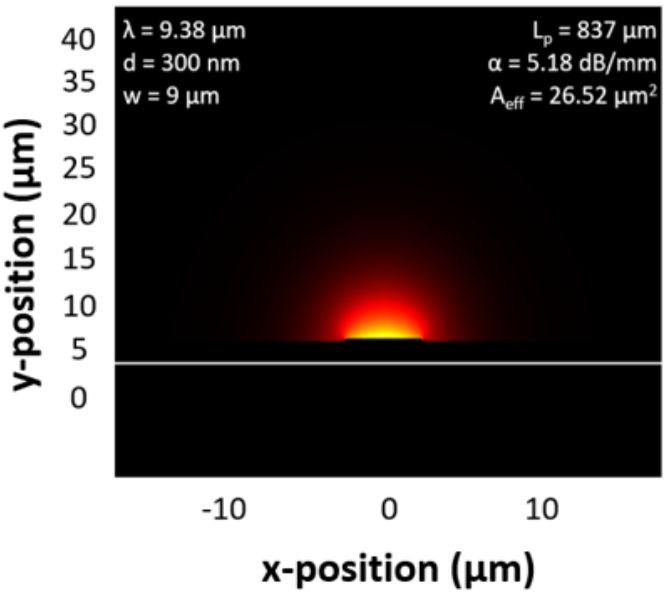

Figure 3.2: Cross-section of the simulated optical mode area at 9.38 µm wavelength. The designed waveguide geometry shows good mode confinement and result in a propagation length of 837 μm. This is suitable for liquid spectroscopy.

The main portion of the optical mode resides in air in such a waveguide configuration, which supports the idea of chemical sensing application with fabricated germanium waveguides Fig. 3.2.

As next step, we analyzed the change in the mode area from the nanometer-scale for the different protective layers . As can be seen in the figure below Fig. 3.3, for wavelengths above 9 μm, the mode area experiences impact from the protective coatings. The mode area is strongly influenced by the choice of material and in case of Al_2O_3 and TiO_2 even improved mode confinement is displayed . The complex refractive index that are used here are obtained from literature [56]. In spectroscopic applications a larger extending mode is more suitable, since it is more sensitive to surrounding medium. Nevertheless, the selection of the most promising material is further investigated, with the additional attenuation of the protective oxide films as figure of merit.

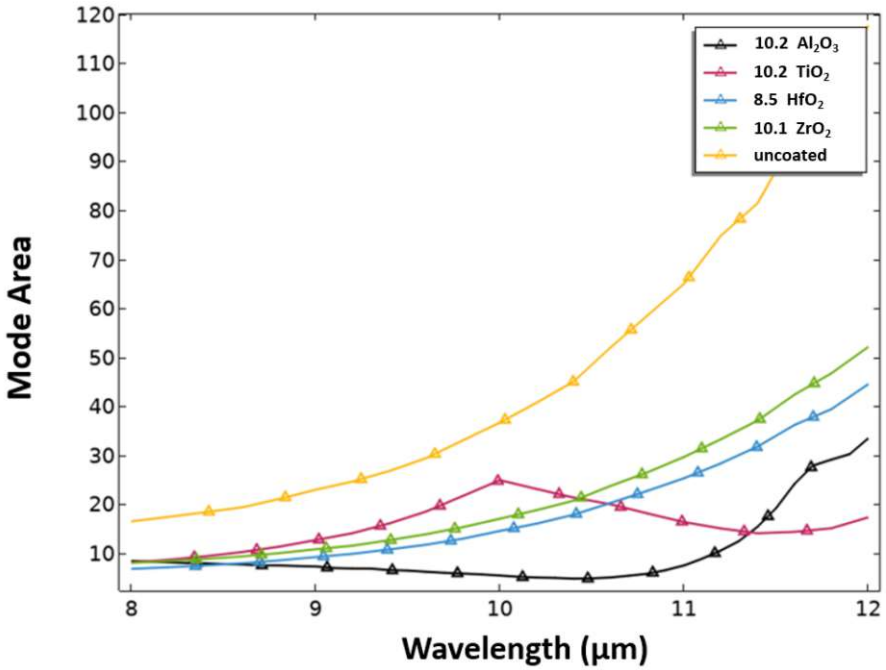

Figure 3.3: FEM simulations of mode area for different ALD-based thin-oxide films in LWIR including: Al_2O_3, ZrO_2, TiO_2, HfO_2 and uncoated Ge/Au as reference. Above 9 μm the mode area of coatings vary, i.e. Al_2O_3 and TiO_2 show improved mode confinement, where ZrO_2 and HfO_2 indicate further increase in mode area.

Attenuation of Thin Oxide Films

The additional losses due the coatings are obtained from the simulations. The choice of materials is determined with their transparency at the wavelength range of interest and being non-hazardous. Hereby, fabrication problems including roughness, inhomogeneities or oxidation levels of the coating material can affect the attenuation. Therefore, in comparison for simulated values coated samples need to be characterized using Atomic Force Microscopy (AFM), see Chapter 4.

As can be seen from Fig. 3.4, additional losses caused by insulator layers are around

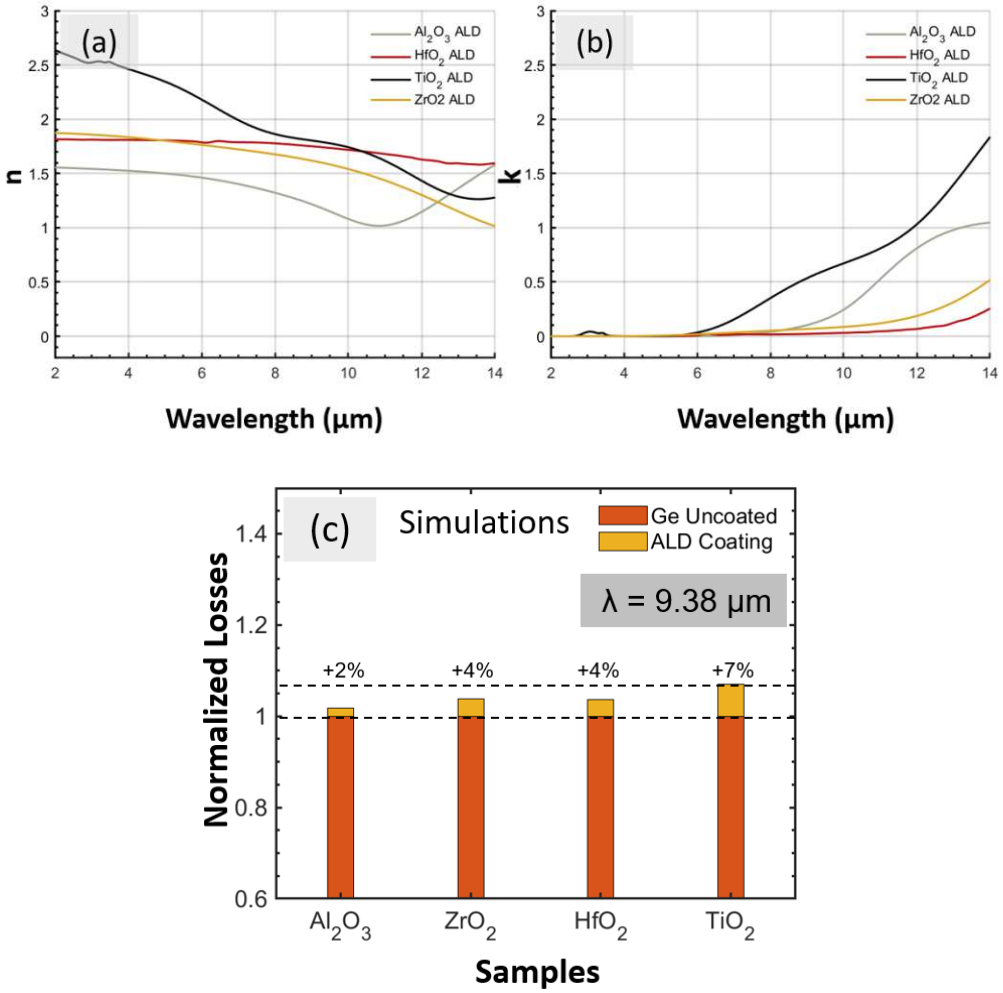

Figure 3.4: (a)-(b) Complex refractive index values from the ellipsometry measurements of thin-oxide films in mid-infrared. (c) Simulated wavelength dependent normalized losses for Ge-based SLSPP waveguides with different thin-oxide films at 9.38 μm wavelength range. Hereby, TiO_2 indicates significant increase in losses, where ZrO_2 and HfO_2 coatings resemble similar results. Al_2O_3 on the other hand performs best compared to the other devices with only a slight increase (+ 2%) in normalized losses.

~2-7 % additional losses for 10 nm layer thickness. Since ALD results in accurate layer thickness and uniformity, we expected the characterization of the waveguides (Section 4.1) to give a similar outcome.

The Propagation Length of Thin Oxide Films

The propagation length decreases with the increasing germanium layer thickness, where all other geometrical parameters remain same. This is because thicker structure result in more confined mode and an increase in mode effective index (n_{eff}), which eventually leads lower propagation length [41]. Moreover, this phenomena covers almost the whole LWIR spectrum (see Fig. 3.5a), indicates that the device can give similar performance in this range.

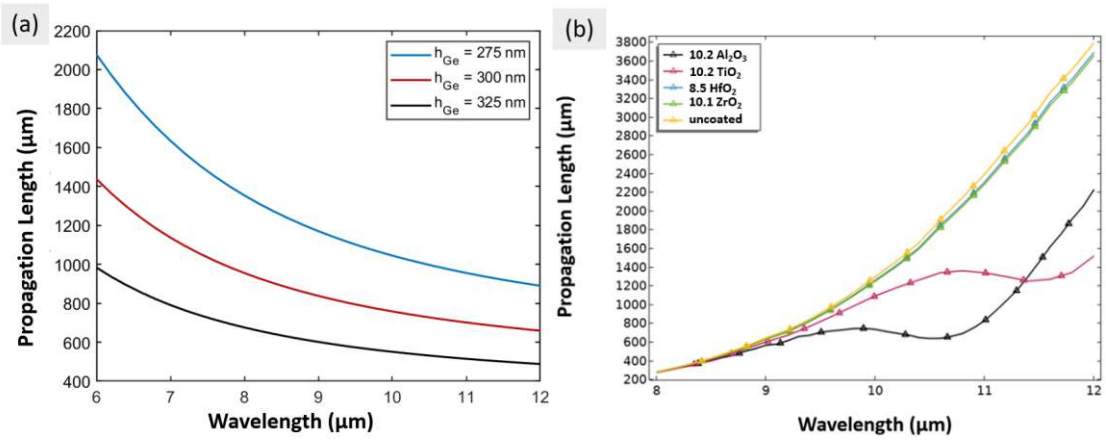

Figure 3.5: (a) FEM simulation shows the impact of different layer thicknesses of germanium on the propagation length. (b) Simulated wavelength dependent propagation length for Ge-based SLSPP waveguides (300 nm Ge stripe with 9 μm width on top of $\sim$ 100 nm Au) with different thin-oxide films in LWIR. Here, the propagation length of germanium is illustrated again (uncoated), resembles to those ZrO_2 and HfO_2 coatings. For TiO_2, after 10.5 μm the propagation length decreases and again increases, where the wavelength is reached 11.7 μm. Al_2O_3 follows also this pattern, but around 10.6 μm wavelength.

The propagation length is related to the attenuation constant and imaginary component of the propagation constant by the formulas (see Eq. 3.1 - 3.2) as we mentioned before. In addition, the attenuation constant α is related to the complex refractive index values (see Fig. 3.4) and therefore it is reflected in the change of the propagation length of the coatings. The decrease in the propagation length of both Al_2O_3 and TiO_2 correlates with the material behavior of these coatings. Another reason might be that the field begins to penetrate inside the metal. The propagation length decreases in the shorter wavelengths, since the fraction of modal power in metal and damping increases. Nevertheless, Figure 3.5 depicts the propagation length of the Ge-based SLSPP waveguide and all the other

coated devices around the same value ($\sim$ 840 μm) at the wavelength of interest (9.38 μm). This further proves a reliable section on the surface of the waveguide, which is large enough for sensing activities.

CHAPTER 4

Experimental Procedures

Optical Setup

The fabricated 1,0, 1.5 and 2.0 mm long germanium waveguides were characterized using the optical setup shown in Fig. 4.1. The laser source is operated in continuous wave (CW) operation at a wavelength of 9.38 μm to excite the plasmonic mode on waveguide. For improving the signal to noise ratio of the measurement we use a beam chopper operated at 525 - 550 Hz together with a lock-in amplifier. This is followed by coupling the light in and out of the waveguide under investigation using two lensses (C037TME-F, Thorlabs). The first lens is focusing the light onto the facet of the plasmonic waveguide, while the second collimates the out coupled mode.

The sample is placed on a custom-made aluminum block to hold the sample and with the help of a vacuum pump to stabilize it during the measurements. The alignement of the waveguide was obtained by placing it to the focal distance of both lenses (f = 340 μm) and checking the right position with the help of a digital microscope ("Dino-Lite Edge" Digital Microscope) Fig. 4.2a. This pre-alignement is supported using a piezoelectric motor to change the position of the sample with nanometer precision on the x- and y-axis see (see Fig. 4.2b). The beam is then aligned to give a good gaussian beam shape on a mid-IR camera using a ZnSe beam splitter and simultaneously on a highly sensitive HgCdTe detector with detectivity 2.0×10^9 cm $\sqrt{Hz}W^{-1}$ at 10.6 μm ("PVI-4TE-10.6", Vigo Systems). The Gaussian beam profile is also confirmed by both, the image on the mid-IR camera connected to a monitor and the signal response from the waveguide measurements. Hereby, to be more precise on characterization of devices, we measured each waveguide at least three times. The detected signal is amplified by using a lock-in-amplifier, which helps increase in the signal-to-noise ratio to obtain better signal response from characterized devices. In order to help with the alignement steps, we implemented a virtual programming code with LabVIEW to monitor resulting changes read by the detector in real time.

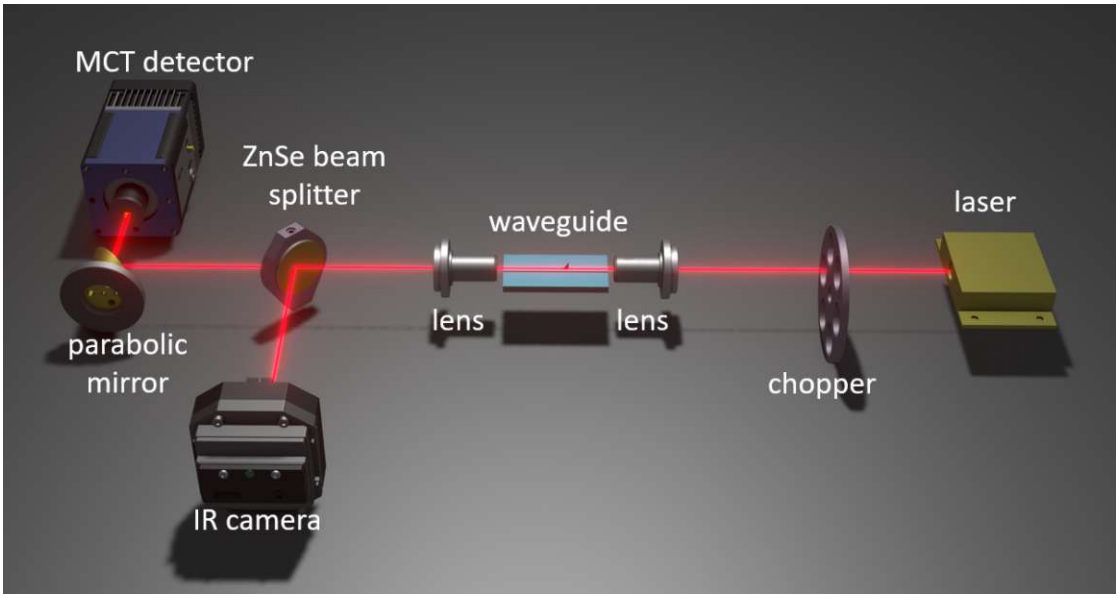

Figure 4.1: Experimental setup for measuring the semiconductor-loaded plasmonic waveguides at 9.38 μm wavelength. The optically chopped CW laser beam from the DFB-QCL is in- and out-coupled onto the Ge/Au-based plasmonic waveguide under investigation using lenses. The pre-alignement of the waveguide is done by using piezo-actuators with high (nanometer) precision. The beam is then analyzed for its 2D profile with the help of a mid-IR camera. Lastly, the beam is focused on a MCT detector and its signal-to-noise ratio is improved by a lock-in amplifier.

The cut-back technique is performed to extract the loss per unit length and coupling efficiency of the waveguides. The method depends on cutting the same waveguide to different lengths and measuring consecutively the same waveguide. This technique assumes that in- and out-coupling facet of the waveguide are identical after cleaving the device to the desired length. Since achieving the same coupling efficiency is almost impossible, instead of cutting the same device several times we used identical waveguides of different lengths as it is demonstrated by Berini et. al. [55]. This has been approved through characterizing the profiles of each device (DekTaK Profilometer) and ensuring the waveguides have similar Ge-layer thickness and width (see Fig. 2.10). Furthermore, corresponding attenuation values in dB of the same waveguide length were controlled to make sure that they indicate similar results even in the presence of small temperature fluctuations of the laser source and alignement dependency during measurements. This is additionally confirmed one more time comparing the linear fit from those measured values and theoretical values, which we obtained from simulations. Lastly, the values of each waveguide are averaged and the method is further applied to different lengths to extract the information of coupling losses. In Chapter 5, a good fitting of simulated and experimental data will be given.

The effect of adding additional thin oxide layer on total losses is determined via

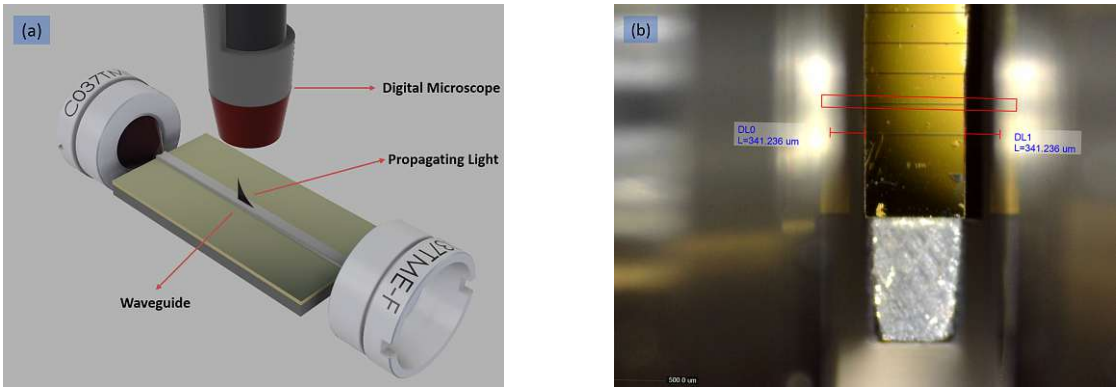

Figure 4.2: (a) Schematic version of the core part of the waveguide characterization setup. The germanium and gold layers are indicated in light grey and gold color. (b) Real-time alignement of the waveguide (image is taken with the digital microscope from the top). The red rectangular spot shows the area where light mode is propagating.

characterizing the same waveguide before and after the coating. As it is performed on the uncoated waveguides each waveguide is measured at least 3 times with measuring and noting down a new reference each time.

One additional method to confirm that the measurement results are in good agreement with those of the simulations is as discussed by checking the optical mode profile by the mid-IR camera and measuring the mode intensity profile (see Fig. 4.3). Once the waveguide is properly aligned to both lenses and the intensity of the signal is confirmed, keeping all the components stable, only the waveguide is moved 20 μm below along the y-axis (into the gold layer and below) using the piezoelectric motor (1 step of motion = 30 nm). Then starting from the same initial point the procedure is repeated and the waveguide is additionally moved in horizontal direction for 3 μm on both sides.

The final measurement is made along the y-axis into the Ge and then air for in total 60 μm. The measured mode power is expected to give an exponential decay through both medias (metal and air) from the interface as we explained in Section 2.0.4. In the next chapter we will compare both: simulated and experimental mode profiles in further detail and we will discuss the coupling losses obtained from the cut-back technique.

Liquid Experiment

This section of the chapter refers to one of the future goals, which is the integration for on-chip sensing applications in the mid-IR using broadband germanium waveguides. Hence, we characterized material behavior of the thin-oxide films in liquid environment to investigate whether this configuration enables protection of the device in water, without dissolving Ge below the thin ALD coatings. In addition, we investigated the agreement between simulated and measured values (see also Section 3).

Firstly, two germanium waveguides without any insulator layer were taken as reference

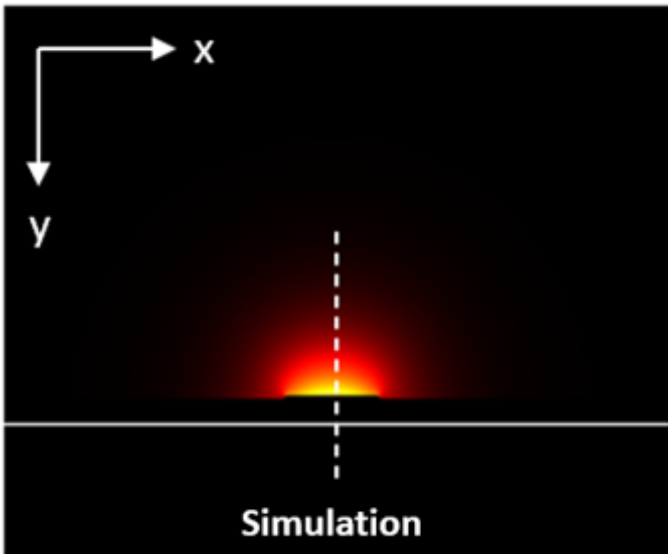

Figure 4.3: Simulated optical mode profile from Ge-based semiconductor loaded waveguides. The white dashed line is representing the spots along y-axis where Gaussian beam profile is investigated.

and their optical losses are calculated through the formula [Chapter 3: $\alpha_{dB/m} = 20\alpha \log e$]. 0 min is indicating the starting point of the experiment where no water is present (see Fig. 4.4). This is followed by submerging the sample at room temperature into a glass beaker filled with DI water to observe solubility of germanium waveguides without additional insulator. Then the samples are inspected after 30 min and 90 min in the water beaker. During this experiment the following individual steps are repeated to analyze the changes after the water submersion: the waveguide profile is measured and optical images are taken with the microscope.

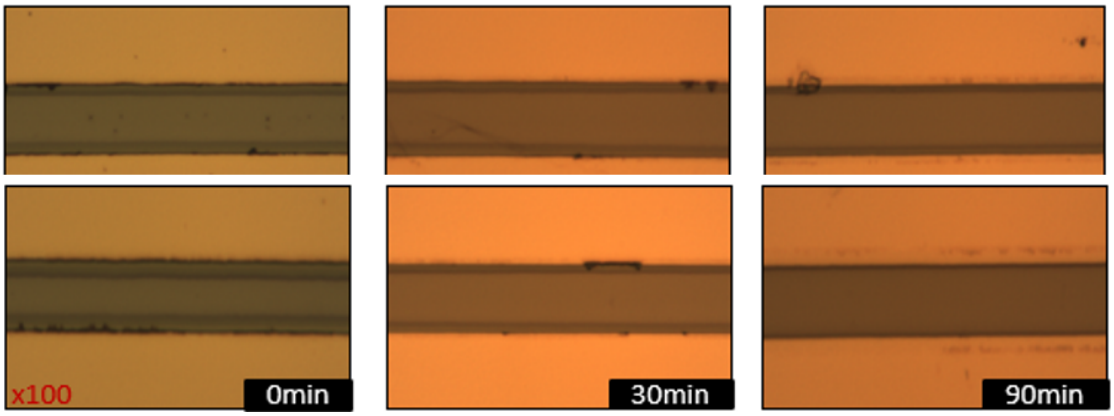

Figure 4.4: Microscopic images of the germanium (reference) waveguides after t = 0, 30, 90 min in water.

Next, other similar samples that have been previously measured with the waveguide setup to obtain their losses are covered with the ALD insulation layers and undergo the same submersion procedure (0 min, 30 min and 90 min - see Fig. 4.6). In the end (after 90 min) they are characterized again in the waveguide setup for optical losses (see Fig. 4.5).

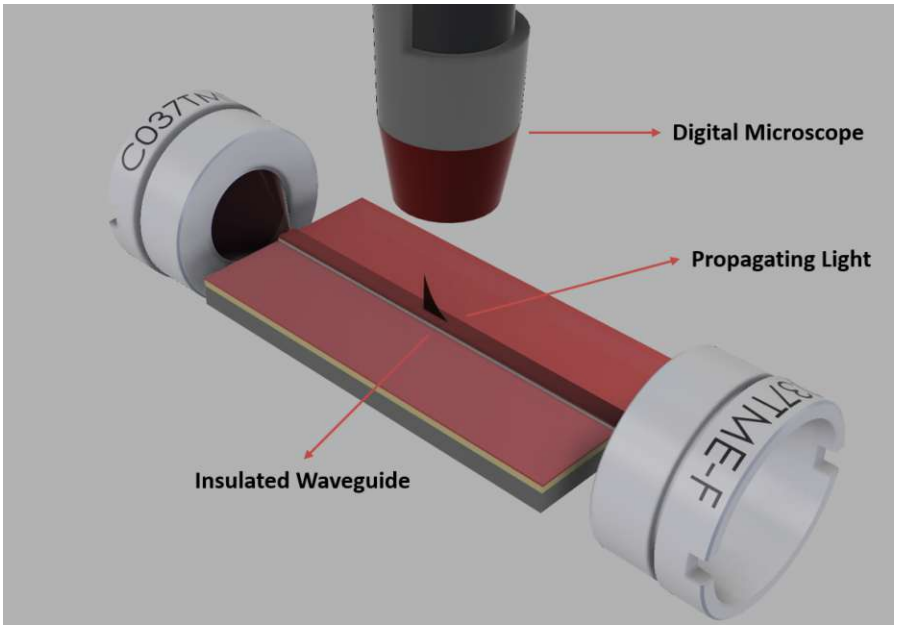

Figure 4.5: Schematic version of characterization of insulated Ge-based SLSPP waveguides. The insulation layer is shown with red color.

It has to be taken into account, that the thin oxide films might also experience impact from the water submersion, which could e.g. result in increased surface roughness together with a change in the total attenuation. Since the dissolution of the coatings in water is expected to be much lower than for germanium, in the best case the same losses should be measured after the submersion experiment. On other hand germanium and its oxide in the presence of H_2O results in degradation of sample and therefore is not stable [28]. As a consequence, the total attenuation of the uncoated samples is expected to be higher than for the coated samples as we will demonstrate in Chapter 5.

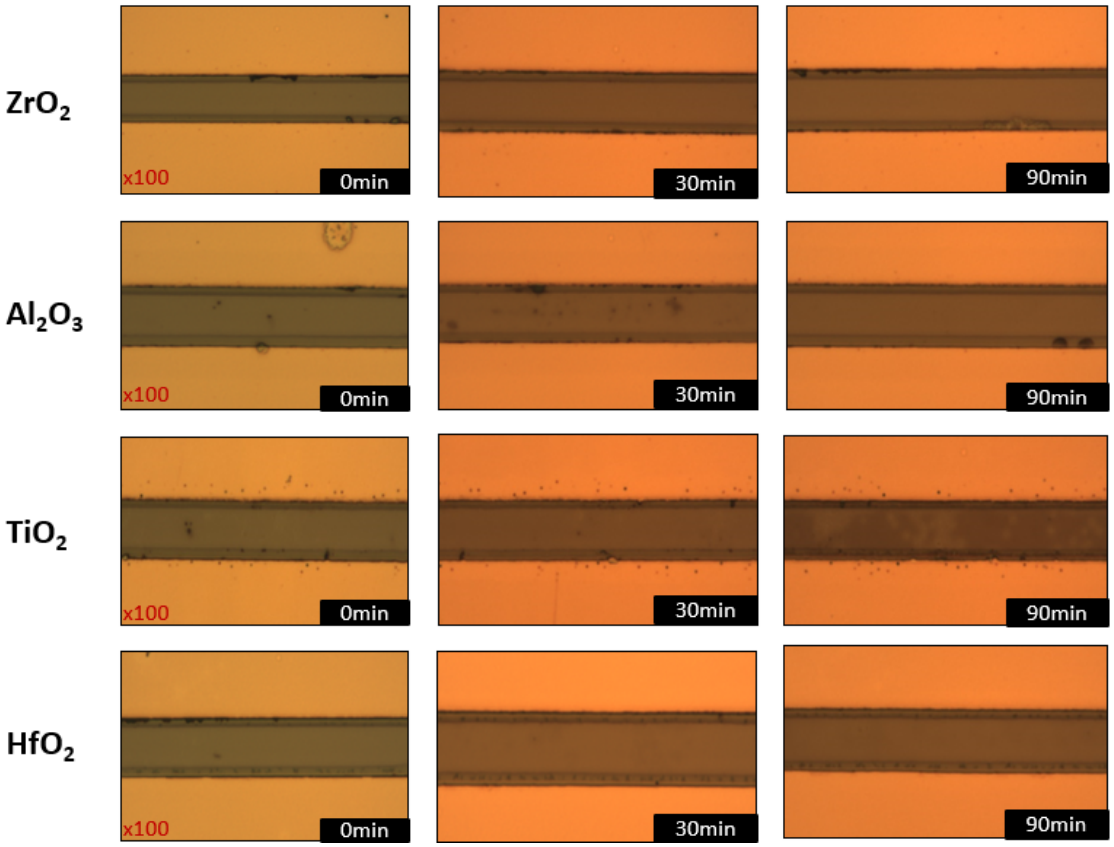

Figure 4.6: Microscopic images of the insulated germanium waveguides after t = 0, 30, 90 min in water.

CHAPTER 5

Results

Before analyzing the degree of protection of ALD coated layers, we characterized the samples with Scanning Electron Microscope (SEM). As can be seen in Fig. 5.1, germanium shows some residuals which can be caused during the lift-off process. On the other hand existence of a liquid indicates increased side wall roughness on Alumina (b) and Zirconia (e), while Titania displays the same as resulted by liftoff. In addition, (b)-(d) show some particles on their surfaces that is difficult to remove with solvents like acetone.

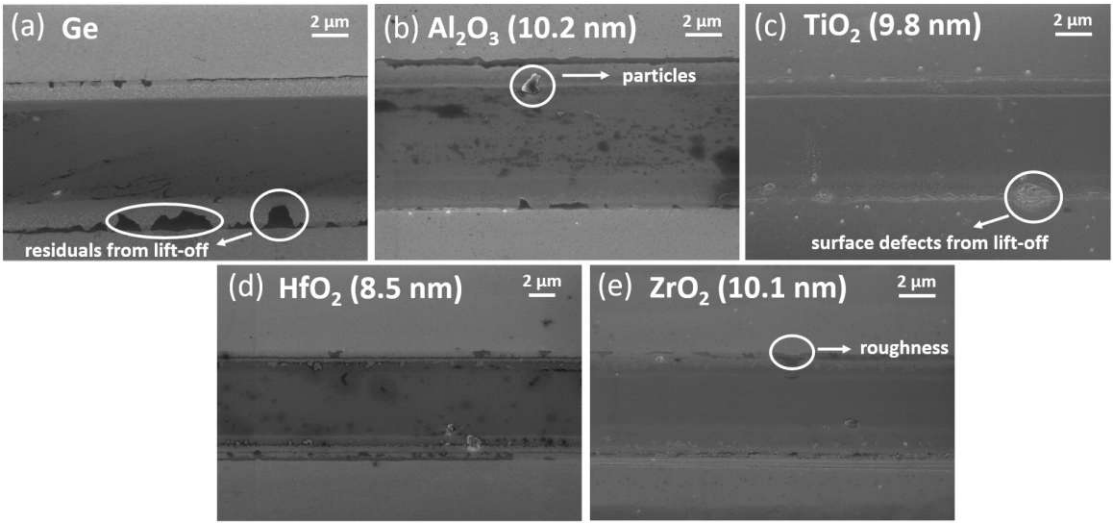

Figure 5.1: SEM images of (a) Germanium-reference sample, (b) Al_2O_3 (10.2 nm), (c) TiO_2 (9.8 nm), (d) HfO_2 (8.5 nm) and (e) ZrO_2 (10.1 nm). In most of the devices good surface quality is displayed, while some defects (i.e. lift-off residuals, particles and sidewall roughness) from the lift-off process can be observed.

A question yet unanswered by our study is the impact of uncontrolled interface reactions

between Ge and the insulator layers. Oxygen based passivations show more promising properties to preventing the diffusion between Ge and a passivation layer [57]. As shown in literature, additional surface treatments like nitridiation [58], NH_3 gas treatment [59] [60] or sulfur-based treatment help to further improve electrical properties [57]. For now as it is demonstrated in the next section, the current coatings fulfill their tasks partly or very well in water.

As we discussed in Section (4.2.). samples were submerged into DI-H_2O to investigate the impact of coatings on waveguide degradation. Since the germanium dioxide is water soluble [61] we expected unprotected Ge waveguides to dissolve over time. Hereby, it is important to mention that this dissolution process highly depends on layer thickness. In our samples Ge layer is approximately 300 nm thick, therefore visible degradation is expected to be seen on the minutes to hour(s) scale.

We tested during this experiment in total 6 samples: 2 uncoated reference samples (Ge waveguides only) and the 4 ALD-coated waveguide chips, one for each type of coating material as follows: Al_2O_3, ZrO_2, TiO_2 and HfO_2. All samples have an initial thickness of 300 nm, but already after the first exposure in water, the uncoated samples show significant reduction in Ge layer thickness by about 30 nm ($\sim$10 % of the initial thickness). Coated samples on the other hand, remained same in layer thickness. After additional 60 min, the uncoated samples showed tremendous change with removal of almost half of the Ge layer. The waveguide profile shape till 30 min of water exposure stays constant (only gets slightly more round at the edges). After 90 min especially one of the two uncoated samples (Fig. 5.2a-b) shows a much more round profile. At this stage there are also some effects visible on the coated samples. TiO_2 and HfO_2 show first degradation effects with a reduction in total layer thickness by about 50 nm, while ZrO_2 and Al_2O_3 remain not effected.

In the case of HfO_2 it is important to mention that the deposited thickness is less than for the other coatings ($\sim$ 8.5 nm). Moreover, passivating germanium dioxide with HfO_2 is especially known to result in charge trapping and fixed charges. [[57],[59], [60]] This process at the Ge - HfO_2 interface could lead to oxidation and consequently the removal of both layers (HfO_2 and Ge) in water. To prevent this problem an additional thin passivation layer of SiH_4 between Ge and HfO_2 can be implemented. Storing Al_2O_3 coated samples for 3 months in air can reduce surface recombination velocity by a factor of 3-4 [62].

The microscope analysis of all samples showed that the submersion has no visible effect on the profilometer measurements that basically also show little to no change in the width of the waveguides (see Fig. 4.4).

The Atomic Force Microscope (AFM) has been applied for advanced characterization of the surface topography of all samples. This measurements further help us to distinguish the more promising coating layers from the unstable ones after the submersion test as it is displayed in Fig. 5.3. Firstly, measurements of uncoated Ge layers resulted in RMS values around 1 nm after 90 min in water, which is similar to results from Chui. et al.

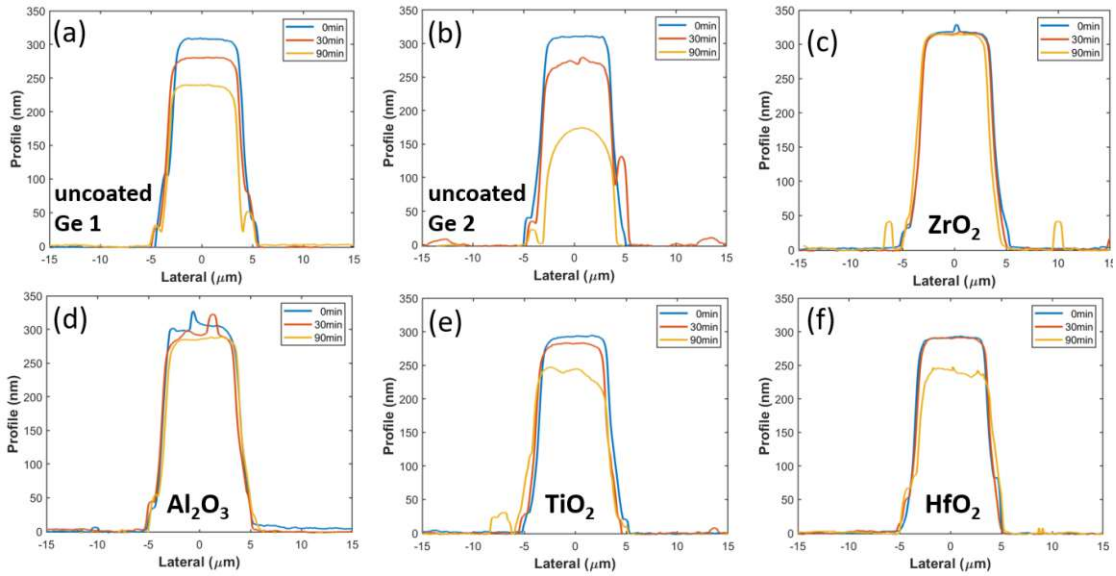

Figure 5.2: Profilometer measurements after the water submersion experiment (pre: blue, 30 minutes: red, 90 minutes: yellow) of: (a)+(b) uncoated waveguides, (c) ZrO_2 (d) Al_2O_3 (e) TiO_2 and (f) HfO_2.

after 5 min DI-H_2O rinsing. [63]. The reason behind it is, the water exposure times more than 60s results in adsorption of H_2O on the surface, forming germanium hydroxides and ultimately leading to increase of the surface roughness [64].

For the coated devices on the other hand surface roughness varies, whereas (d) HfO_2 and (e) ZrO_2 show similar values, they are significantly higher for (b) Al_2O_3 and (c) TiO_2. In case of HfO_2 and ZrO_2 it is relatively close to the RMS value without previous submersion in H_2O [65]. But the fact that degradation can still occur in some of the samples yields the conclusion that further test would be helpful to better understand this (e.g. using thicker ALD coatings, other Ge samples to investigate for surface roughness effects from Ge, etc.).

A more detailed investigation of the surface topography gives us additional information of the fabrication process. Some dirt particles can be observed on the surface probably from the lift-off step. The layer inhomogeneity in Al_2O_3 coating can be caused from the underlying sputtered Ge layer. Only in case of the TiO_2 coating a pinhole is present on the surface, indicating a possible point where the water might penetrate and attack the coating over time. Defects on the coating surfaces distinguish Al_2O_3 and TiO_2 from the others Fig. 5.4, but the final choice of coating layer for passivation of Ge waveguides also strongly depends on the measured optical losses.

One important characteristic of the waveguide is the attenuation or loss, that a light wave experiences as it travels through the waveguide. Since interaction of the propagating waves with the surface is the basic mechanisms of guiding, its quality is of critical

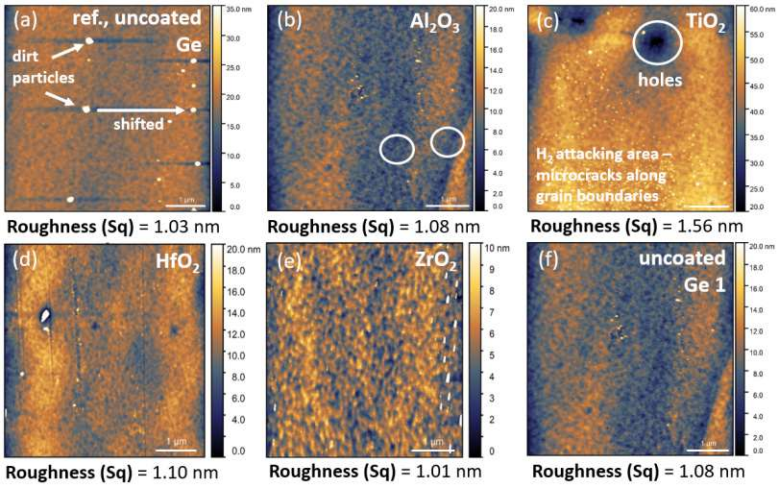

Figure 5.3: AFM analysis of the coated vs uncoated waveguides after 90 minutes submersion in water: (a) Germanium reference (no submersion) only, (b) Al_2O_3 (10.2 nm), (c) TiO_2 (9.8 nm), (d) HfO_2 (8.5 nm) and (e) ZrO_2 (10.1 nm), (f) Germanium only (after submersion). The RMS roughness is given for each sample, while some particles, non-uniformity and holes can also been observed and are indicated.

importance. [66]. Before characterizing the optical losses of Ge coated and uncoated devices, we identified the Gaussian beam profile propagating along the waveguide. This is achieved in three steps as following, first the beam profile on mid-infrared camera is checked to prove that the alignement is correct and there is no interference effect. Secondly, the waveguide under investigation is placed to the focal point of the lenses and their position is confirmed by digital microscope. This is followed by positioning the waveguide with the help of the piezoelectric motor 6 μm below the dielectric-air interface, which is set as origin point. Finally, propagating mode intensity is measured while changing the position of waveguide on y-axis from origin (below the metal) to the air. As it is demonstrated in the Fig. 5.5, the Gaussian beam profile that we measured resembles to a certain degree the simulation result. A wider measured profile can be expected, because we measure the convolution with the initial beam diameter of the $\sim$ 9.4 μm laser emission.

The Gaussian beam profile denotes significant portion of the propagating optical mode is in air, which is one of the advantages for spectroscopic applications. The fabrication imperfections on the material system results additional scattering losses and therefore Gaussian beam profile differs in between simulated and measurement values.

The performance of such waveguides are characterized by their total attenuation (or simply their propagation length) when all relevant loss mechanisms are considered Section (2.0.4). The underlying assumption of the facets of waveguides with different lengths to be identical is verified by the linear fit data as it is given in Fig. 5.6.

From Fig. 5.6. we measured loss coefficients as 17.28$\pm$1.20 dB, 14.85$\pm$0.96 dB and

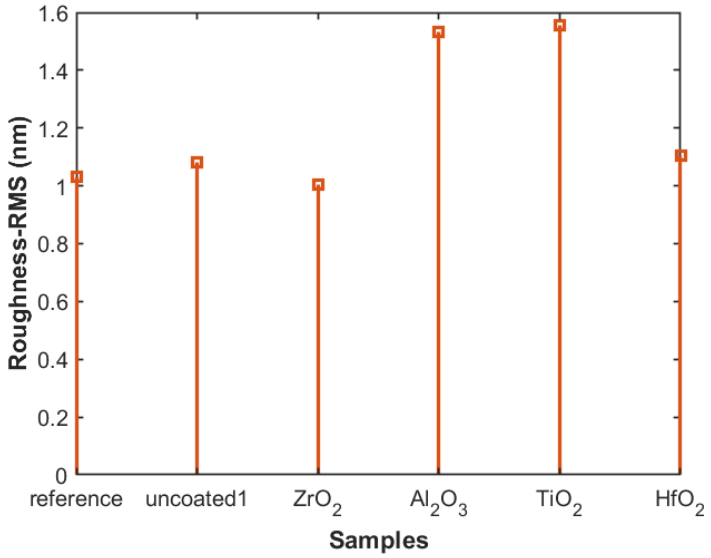

Figure 5.4: RMS roughness values after submerging samples into H_2O for 90 min. The samples displayed here are including two uncoated Ge reference samples and four ALD-coated samples: ZrO_2, Al_2O_3, TiO_2 and HfO_2.

14.36±0.99 dB for 1.0, 1.5 and 2.0 mm devices (width $\sim$ 9 μm, thickness $\sim$ 300 nm). Propagation length of germanium on gold waveguide is defined from simulations in Section 3 as L_p of 837 μm. The experimentally extracted coupling losses from devices are 5.18 dB/mm, which gives good agreement with previous measured values from literature [41]. As mentioned before, waveguide losses (material + scattering losses) exhibits the surface quality of the waveguides since the propagating mode is acting on the interface and hereby it indicates the value of 12.02 dB/mm. Again this agrees well with our previous work and it can be even easily improved with changing some steps during fabrication (i.e. etching instead of lift-off) [41].

Here again, gold deposition by sputtering can vary the expected device parameters. Since the vertical mode size is dependant on metal layer in DLSPP waveguides, controlling the variation in thickness will lead better results. During the liftoff process film thickness can be attributed as less tolerance [67] but, it can be easily improved by replacing that step with a Reactive Ion Etching (RIE) process. Hereby, it should be mentioned that the mode field diameter (distance between the outermost $1/e^2$ points of the intensity) differs [68], if the operating wavelength is higher than Ge waveguide width. This changes the guiding mode property and leads to additional coupling losses.

The demonstrated DLSPP waveguides presented in this work show lower losses than some proposed theoretical concepts like heavily doped semiconductors [69], germanides [70] and silicides [71] based SLSPP waveguides. Our devices so far also cover almost the whole LWIR spectrum ($\sim$ 5.6 - 11.2 μm [41]), which makes them superior regarding the

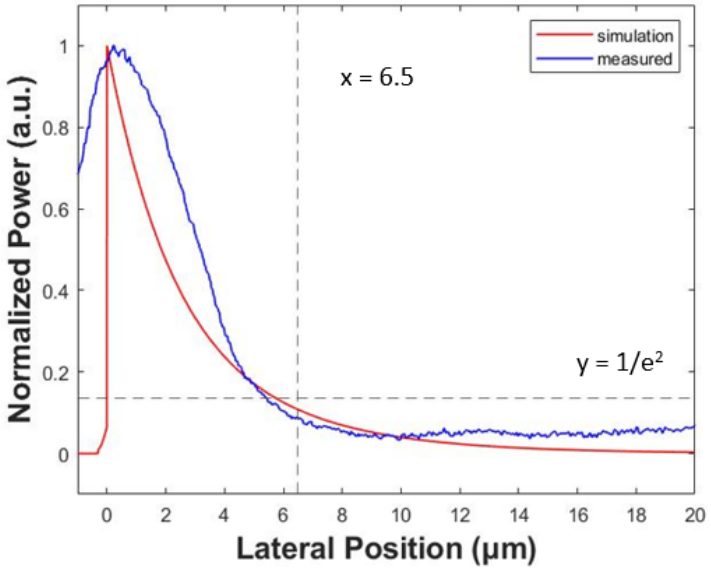

Figure 5.5: Gaussian beam measurements (blue) in comparison with simulated values (red).

flexibility in liquid sensing measurements. Considering the simplicity of fabricating of such devices, this waveguide architecture can be straightforward implemented on photonic integrated device systems.

As final step of characterization, we present the losses without coating, with coating and after the submerging experiment to evaluate their material dependent effects, shown in Fig. 5.7. The uncoated samples display significant increase in their losses, which also agrees well with decrease in their layer thickness. This can be seen even better for sample "uncoated2", since it has lost almost half of its layer after 90 min exposure in water as we previously discussed. The ALD coated samples on the other hand, have shown that for ZrO_2 and Al_2O_3 almost no change in losses occur (∼10-13 % additional losses with insulating them), demonstrating the excellent protective capabilities of the ALD coatings. For TiO_2 and HfO_2 interestingly we observed some increase in losses, but this we believe can be eliminated with the increase of their layer thickness. Especially, wide range applications in electronic devices of HfO_2 and the promising results of this material in III-V MOS gate stacks as high k-material [72] makes it still a good candidate for our future research. This again agrees well with the reduction in their profile as we discussed previously. The ZrO_2 and Al_2O_3 coated devices after water exposure also display great performance with minor increase in their losses (∼0.71-0.82 % additional losses). After the characterizations we can conclude that robust protective capabilities of ZrO_2 and Al_2O_3 make them possible candidates of chemical and biological experiments.

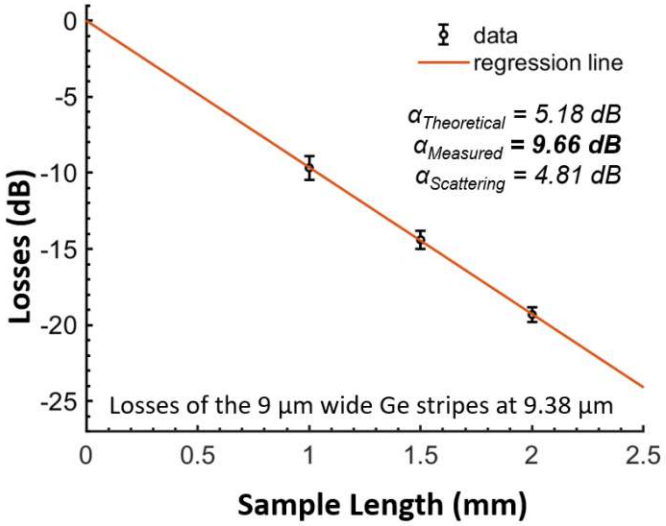

Figure 5.6: Cut-Back technique is applied to determine the coupling losses of Ge-waveguides at 9.38 μm wavelength. Each one of the black data points represent the averaged total attenuation losses for different device lengths including the corresponding error bars.

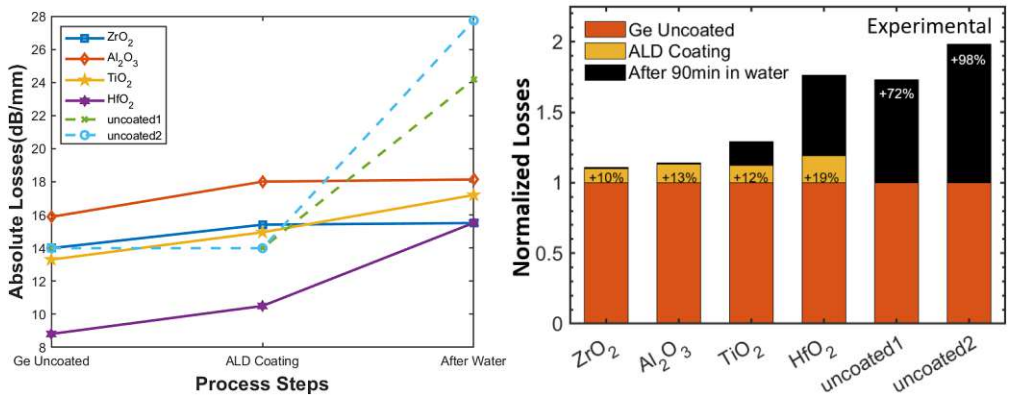

(a) (b)

Figure 5.7: Total attenuation of waveguides before and after the ALD coating and after the submergion experiment: (a) absolute losses (dB/mm) and (b) normalized losses. Deposition of coatings added 1-2 dB/mm, which differs from the simulation data, shown in Fig. 3.4. The water exposure increases losses of uncoated devices significantly as well as for TiO_2 and HfO_2 samples to a lesser degree. This again proves that thickness of the oxide films can be still increased to a certain degree for better protection.

CHAPTER 6

Conclusion

In this thesis work, we aimed to develop a new material concept with Ge/Au-based plasmonic device for liquid spectroscopy at mid-infrared wavelength. The fact that germanium dissolves under water exposure over time, several high quality insulation layers are coated by ALD to prevent it from happening.

We demonstrated experimentally, a single mode (transverse magnetic) semiconductor loaded surface plasmon polarition (SLSPP) waveguide with low optical losses (<15 dB/mm) at 9.38 μm. Besides, it is shown that fabricated waveguides are operational at a full octave in the LWIR range between 5.6 μm - 11.2 μm [41]. It was shown with simulations that a significantly big portion of mode (>96%) is guided outside the waveguide and resides in the surrounding medium. In addition, the propagation length of our device exceeds 800 μm, giving us high flexibility for on-chip spectroscopy-based applications. It is possible to further optimize that by balancing the trade-off between propagation length and mode confinement through adjusting the geometry of SLSPP waveguides.

As insulation layer, several nanometer thick ($\sim$ 10 nm) metal oxide fims are deposited by ALD, including Al_2O_3, ZrO_2, TiO_2 and HfO_2. We analyzed the performance of our devices in liquid by submerging all 6 samples: 2 uncoated reference samples (Ge waveguides) and the 4 additional ALD-coated samples into DI-H_2O for 90 min. The surface topography of both coated-uncoated samples are investigated by atomic force microscope (AFM) and scanning electron microscope (SEM). The additional coatings result in increase of optical losses by about 10% (i.e. 1-2 dB/mm). After the water exposure, uncoated samples showed a major increase, which agrees well with decrease in their layer thickness. Herein, ZrO_2 and Al_2O_3 display excellent performance with minor increase in their losses by 0.71-0.82 %. TiO_2 and HfO_2 on the other hand, show less good protection (reduction of Ge+coating layer thickness by 50 nm) and more increase in optical losses (i.e. 5 dB/mm for HfO_2).

In the last decades, plasmonic sensors attracted huge interest thanks to their opportunity to confine light to sub-wavelength scale and relatively long propagation lengths. When combined with quantum cascade laser (QCL) technology, they can offer new sensing systems. After the characterizations we can conclude that robust protective capabilities of ZrO_2 and Al_2O_3 make them possible candidates of chemical and biological experiments.

CHAPTER 7

Outlook

In last decades since the initial demonstration of subwavelength light confinement by structuring metals, plasmonics have become one of the pillar parts in the field of sensing and communication.

Despite the remarkable advances, the current state of the art waveguide still requires adaptations on protective layers, before implementing them in on-chip sensing platform (see Chapter 5). This can be easily overcome by a straightforward fabrication procedure of several waveguides with different coating thicknesses and examining them after water exposure like we demonstrated. Indeed, an important drawback will be the increase in total attenuation (see Chapter 3) but, we expect that the new devices perform better in liquid. In addition, functionalization of the final devices enables us to carry out experiments with different biological and chemical substances (i.e. proteins or glucose). I believe that simplicity of our approach provide us here a huge advantage in fabrication and characterization compare to the other sensors presented in literature.

An initial step towards on-chip sensing platform is shown in 2014 with integration of QCL, QCD and SiN_x based DLSPP waveguide on same chip in our group [40]. This is further improved in 2022, by analyzing temperature-induced conformational changes of the model protein bovine serum albumin in heavy water [8]. In this thesis, I presented a series of experimental studies (Chapter 2 - 5), which I believe, have made important contributions to the new plasmonic based biosensors. Recently, we investigated functionalization of the waveguide with some of the devices introduced in this work. Importantly, these recent achievements are creating different platforms for cost-efficient photonic integrated sensing applications.

In addition, I am particularly interested in finding different material concepts for plasmonics and integrated photonics for optical communication. For example, during this project we also studied a replacement for gold with palladium and germanium with polyethylene. Especially, polyethylene is a promising solution for realization of compact

and cost efficient devices. Moreover, SPP-based platforms offer deep subwavelength rather not in the mid-infrared operation and as an alternative approach they can be combined with metawaveguides (guiding section) and other photonic components (i.e. harmonic mixers, modulators, antennas) to address compact planar wireless comunication systems [27]. Another approach would be, monolithic on-chip QCLD based heterodyne detectors for data communication, shown in Fig. 7.1. All this potential technological developments have highly interdisciplinary character covering physics, optics, chemistry, materials science and as well as biology and computer science, makes the field of photonics much more interesting.

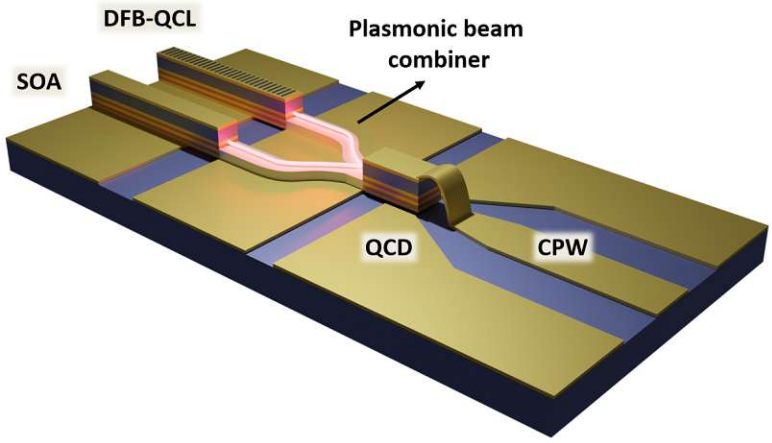

Figure 7.1: Schematic of one of the future monolithic on-chip QCLD based heterodyne detector. Here, semiconductor optical amplifier (in-coupling light is not presented) and local oscillator (DFB-QCL) are the light emitting components of the device. Transmitted signal is guided by PE-based surface plasmon polariton waveguide in the middle section. Then, in the QCD absorbed photons from the obtained beating signal excite electrons and by cascading they give rise to a photocurrent.

CHAPTER 8

LabVIEW Software for Measuring Waveguides

The experimental setup of measuring the SLSPPWs is shown in Fig. 8.1. The optical signal of a 9.38 μm laser is first coupled to the waveguide structure with the help of the focusing lens (see Chapter 4) then out-coupled and collected by the MCT-detector. Lastly, the detected signal is amplified by lock-in amplifier and through the General Purpose Interface Bus (GPIB) connection the signal is read by the software. The system was built around a computer running application based on National Instruments' graphic programming language LabVIEW. According to the requirement of the measurement system, the application includes data communication, data processing, data display and data storage.

Since LabVIEW is a virtual programming environment, it relies on graphical symbols rather than textual language to define a programm's actions. The functions are executed only after receiving the necessary data, means that it is based on dataflow. The program consists of virtual instruments (VIs), which are the representation of actual physical instruments and often imitate their operation as well [73].

A VI consists of three main parts: a front panel for displaying the data to a user, a block diagram as a source code and an icon to represent the VI pictorial. Our measurement VI is structure in two main parts: a read-out programm and a data logging programm. The read-out program for lock-in amplifier has one while loop, illustrated in Fig. 8.2. GPIB address is assigned to 12 as specified by the device and sends data in 200 bytes (bottom center). Then, the data is transmitted to the shift register (right), which sends back data to the loop. The reason behind it is to pass several data by `mean value.vi` to average them for measurement consistency. Then, data is displayed by the function named `LockinAmplifier` in a graph on the front panel for user interaction.

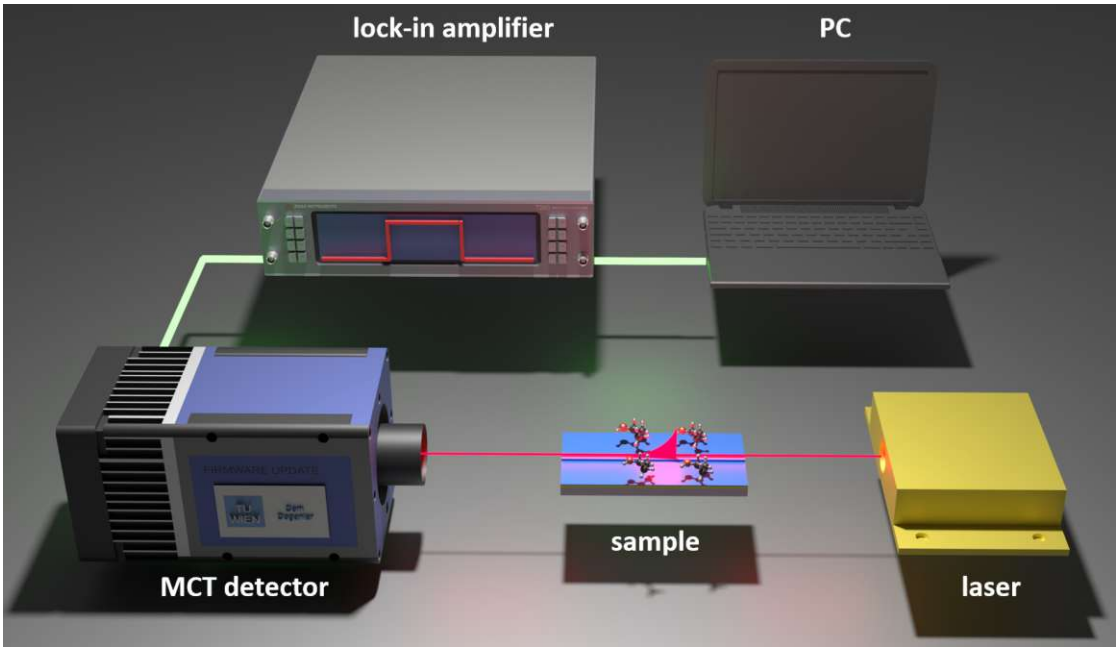

Figure 8.1: Schematic layout of the experimental setup for measuring the semiconductor-loaded plasmonic waveguides at 9.38 μm wavelength. Here, the red line represents the optical measurement signal from the waveguide and the green line shows the data communication line between the detector and PC.

The data logging programm has one while loop and one case structure, is shown in Fig. 8.3. On the left, the call to the function named `Get Date/Time in Seconds` is reveiving the starting time of meaurement from PC. Next in data flow, the acquired time is converted to the string by `Format Date/Time String` function for being written on a file later. Then, last function on this section named `Open/Create/Replace File` is creating the text file for measurement data with the defined starting time and file location. In the center, the while loop iterates the execution after waiting every 5 ms. The logging condition is connected to the case structure, requires the log data button to be pressed by the user. Inside of the case structure, there are two important functions for writing the measurement data to file: `Voltage Output` and `Write Text to File` functions. In color orange displayed `Voltage Output` function is a VI Server reference, means that it refers to the values taken from another function. Here, the data is received from the `Voltage Output` function inside the read-out programm. Finally, the function `Write Text to File` stores all the data to the choosen file path and whenever stop logging condition is met, the software immediately terminates the programm.

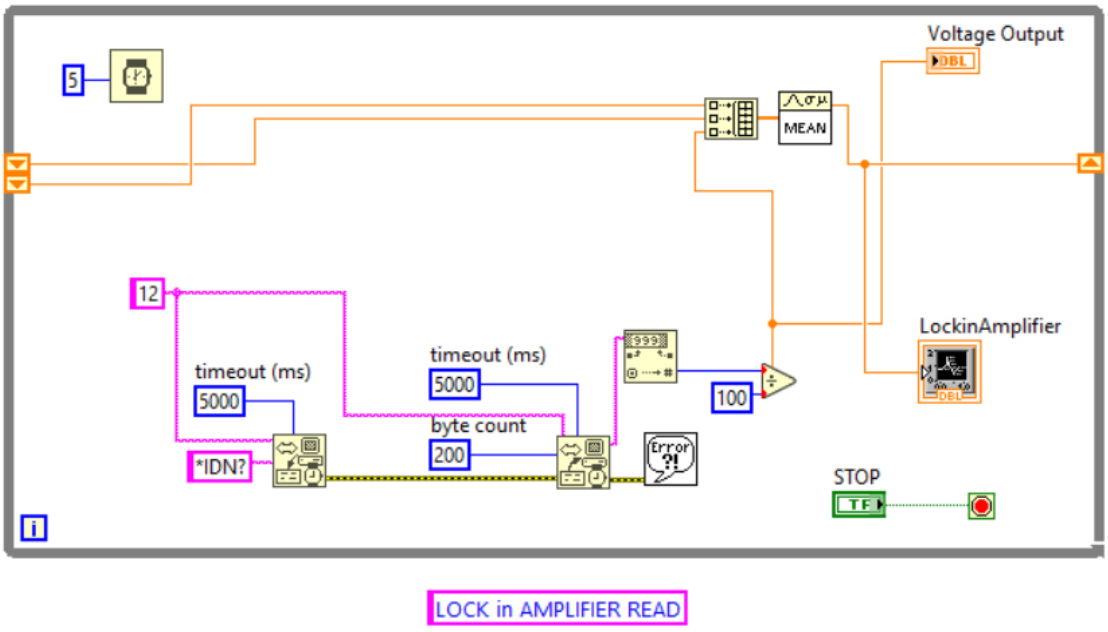

Figure 8.2: Block diagram clipping responsible for reading out the real-time measurement data.

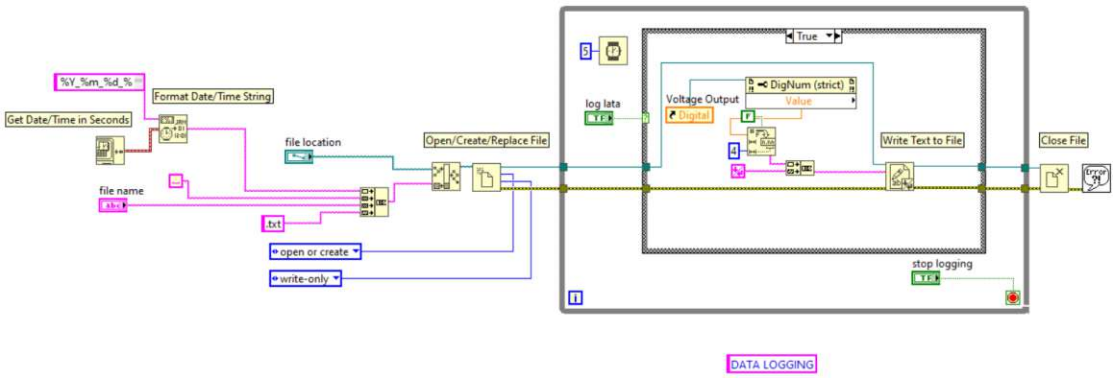

Figure 8.3: Screenshot of the block diagram responsible for logging the measured data by read-out programm.

List of Figures

List of Tables

Bibliography

[1] Boris Mizaikoff. Waveguide-enhanced mid-infrared chem/bio sensors. *Chemical Society Reviews*, 42(22):8683–8699, 2013.

[2] Frank K Tittel, Dirk Richter, and Alan Fried. Mid-infrared laser applications in spectroscopy. In *Solid-state mid-infrared laser sources*, pages 458–529. Springer, 2003.

[3] Nathalie Picqué and Theodor W Hänsch. Mid-ir spectroscopic sensing. *Optics and Photonics News*, 30(6):26–33, 2019.

[4] JR Haynes and W Shockley. The mobility and life of injected holes and electrons in germanium. *Physical Review*, 81(5):835, 1951.

[5] Benedikt Schwarz. *Monolithic integration of mid-infrared photonics*. PhD thesis, Wien, 2015.

[6] Hongtao Lin, Zhengqian Luo, Tian Gu, Lionel C Kimerling, Kazumi Wada, Anu Agarwal, and Juejun Hu. Mid-infrared integrated photonics on silicon: a perspective. *Nanophotonics*, 7(2):393–420, 2018.

[7] Yu-Chi Chang, Philip Wägli, Vincent Paeder, Alexandra Homsy, Lubos Hvozdara, Peter van der Wal, Joab Di Francesco, Nico F de Rooij, and Hans Peter Herzig. Cocaine detection by a mid-infrared waveguide integrated with a microfluidic chip. *Lab on a Chip*, 12(17):3020–3023, 2012.

[8] Borislav Hinkov, Florian Pilat, Laurin Lux, Patricia L Souza, Mauro David, Andreas Schwaighofer, Daniela Ristanić, Benedikt Schwarz, Hermann Detz, Aaron M Andrews, et al. A mid-infrared lab-on-a-chip for dynamic reaction monitoring. *Nature communications*, 13(1):1–10, 2022.

[9] Stephanie Law, Viktor Podolskiy, and Daniel Wasserman. Towards nano-scale photonics with micro-scale photons: the opportunities and challenges of mid-infrared plasmonics. *Nanophotonics*, 2(2):103–130, 2013.

[10] William L Barnes, Alain Dereux, and Thomas W Ebbesen. Surface plasmon subwavelength optics. *nature*, 424(6950):824–830, 2003.

[11] Anatoly V Zayats, Igor I Smolyaninov, and Alexei A Maradudin. Nano-optics of surface plasmon polaritons. *Physics reports*, 408(3-4):131–314, 2005.

[12] Dmitri K Gramotnev and Sergey I Bozhevolnyi. Plasmonics beyond the diffraction limit. *Nature photonics*, 4(2):83–91, 2010.

[13] Alexandre G Brolo. Plasmonics for future biosensors. *Nature Photonics*, 6(11):709–713, 2012.

[14] Ekmel Ozbay. Plasmonics: merging photonics and electronics at nanoscale dimensions. *science*, 311(5758):189–193, 2006.

[15] Gururaj V Naik, Jongbum Kim, and Alexandra Boltasseva. Oxides and nitrides as alternative plasmonic materials in the optical range. *Optical materials express*, 1(6):1090–1099, 2011.

[16] Gururaj V Naik, Jeremy L Schroeder, Xingjie Ni, Alexander V Kildishev, Timothy D Sands, and Alexandra Boltasseva. Titanium nitride as a plasmonic material for visible and near-infrared wavelengths. *Optical Materials Express*, 2(4):478–489, 2012.

[17] S Law, DC Adams, AM Taylor, and D Wasserman. Mid-infrared designer metals. *Optics express*, 20(11):12155–12165, 2012.

[18] Stefan A Maier et al. *Plasmonics: fundamentals and applications*, volume 1. Springer, 2007.

[19] Lev Davidovich Landau, JS Bell, MJ Kearsley, LP Pitaevskii, EM Lifshitz, and JB Sykes. *Electrodynamics of continuous media*, volume 8. elsevier, 2013.

[20] Harry A Atwater and Albert Polman. Plasmonics for improved photovoltaic devices. *Materials for sustainable energy: a collection of peer-reviewed research and review articles from Nature Publishing Group*, pages 1–11, 2011.

[21] Kathryn M Mayer and Jason H Hafner. Localized surface plasmon resonance sensors. *Chemical reviews*, 111(6):3828–3857, 2011.

[22] Eliza Hutter and Janos H Fendler. Exploitation of localized surface plasmon resonance. *Advanced materials*, 16(19):1685–1706, 2004.

[23] Clemens Burda, Xiaobo Chen, Radha Narayanan, and Mostafa A El-Sayed. Chemistry and properties of nanocrystals of different shapes. *Chemical reviews*, 105(4):1025–1102, 2005.

[24] Nanfang Yu, Qi Jie Wang, Mikhail A Kats, Jonathan A Fan, Suraj P Khanna, Lianhe Li, A Giles Davies, Edmund H Linfield, and Federico Capasso. Designer spoof surface plasmon structures collimate terahertz laser beams. *Nature materials*, 9(9):730–735, 2010.

[25] Christopher R Williams, Steven R Andrews, SA Maier, AI Fernández-Domínguez, L Martín-Moreno, and FJ García-Vidal. Highly confined guiding of terahertz surface plasmon polaritons on structured metal surfaces. *Nature Photonics*, 2(3):175–179, 2008.

[26] Xu Chen and Wenhui Fan. Ultrasensitive terahertz metamaterial sensor based on spoof surface plasmon. *Scientific reports*, 7(1):1–8, 2017.

[27] Hao Chi Zhang, Le Peng Zhang, Pei Hang He, Jie Xu, Cheng Qian, Francisco J Garcia-Vidal, and Tie Jun Cui. A plasmonic route for the integrated wireless communication of subdiffraction-limited signals. *Light: Science & Applications*, 9(1):1–9, 2020.

[28] Yinghui Guo, Zuojun Zhang, Mingbo Pu, Yijia Huang, Xiong Li, Xiaoliang Ma, Mingfeng Xu, and Xiangang Luo. Spoof plasmonic metasurfaces with catenary dispersion for two-dimensional wide-angle focusing and imaging. *Iscience*, 21:145–156, 2019.

[29] Anastasia Rusina, Maxim Durach, and Mark I Stockman. Theory of spoof plasmons in real metals. *Applied Physics A*, 100(2):375–378, 2010.

[30] Seong-Han Kim, Sang Soon Oh, Kap-Joong Kim, Jae-Eun Kim, Hae Yong Park, Ortwin Hess, and Chul-Sik Kee. Subwavelength localization and toroidal dipole moment of spoof surface plasmon polaritons. *Physical Review B*, 91(3):035116, 2015.

[31] Hassan Kaatuzian and Ahmad Naseri Taheri. Applications of nano-scale plasmonic structures in design of stub filters—a step towards realization of plasmonic switches. In *Photonic Crystals*, page 93. BoD-Books on Demand, 2015.

[32] John David Jackson. Classical electrodynamics, 1999.

[33] RF Oulton, G Bartal, DFP Pile, and Xiang Zhang. Confinement and propagation characteristics of subwavelength plasmonic modes. *New Journal of Physics*, 10(10):105018, 2008.

[34] Heinz Raether. Surface plasmons on smooth surfaces. *Surface plasmons on smooth and rough surfaces and on gratings*, pages 4–39, 1988.

[35] Andreas Otto. Excitation of nonradiative surface plasma waves in silver by the method of frustrated total reflection. *Zeitschrift für Physik A Hadrons and nuclei*, 216(4):398–410, 1968.

[36] Erwin Kretschmann and Heinz Raether. Radiative decay of non radiative surface plasmons excited by light. *Zeitschrift für Naturforschung A*, 23(12):2135–2136, 1968.

[37] B Hecht, H Bielefeldt, L Novotny, Y Inouye, and DW Pohl. Local excitation, scattering, and interference of surface plasmons. *Physical review letters*, 77(9):1889, 1996.

[38] Tobias Holmgaard and Sergey I Bozhevolnyi. Theoretical analysis of dielectric-loaded surface plasmon-polariton waveguides. *Physical Review B*, 75(24):245405, 2007.

[39] B Steinberger, A Hohenau, H Ditlbacher, AL Stepanov, A Drezet, FR Aussenegg, A Leitner, and JR Krenn. Dielectric stripes on gold as surface plasmon waveguides. *Applied Physics Letters*, 88(9):094104, 2006.

[40] Benedikt Schwarz, Peter Reininger, Daniela Ristanić, Hermann Detz, Aaron Maxwell Andrews, Werner Schrenk, and Gottfried Strasser. Monolithically integrated mid-infrared lab-on-a-chip using plasmonics and quantum cascade structures. *Nature communications*, 5(1):1–7, 2014.

[41] Mauro David, Alicja Dabrowska, Masiar Sistani, IC Doganlar, Erik Hinkelmann, Hermann Detz, WM Weber, Bernhard Lendl, Gottfried Strasser, and Borislav Hinkov. Octave-spanning low-loss mid-ir waveguides based on semiconductor-loaded plasmonics. *Optics Express*, 29(26):43567–43579, 2021.

[42] Zhanghua Han, Liu Liu, and Erik Forsberg. Ultra-compact directional couplers and mach–zehnder interferometers employing surface plasmon polaritons. *Optics communications*, 259(2):690–695, 2006.

[43] Robert Charbonneau, Nancy Lahoud, Greg Mattiussi, and Pierre Berini. Demonstration of integrated optics elements based on long-ranging surface plasmon polaritons. *Optics Express*, 13(3):977–984, 2005.

[44] SI Bozhevolnyi, VS Volkov, E Devaux, J-Y Laluet, and TW Ebbesen. Channelling surface plasmons. *Applied Physics A*, 89(2):225–231, 2007.

[45] Valentyn S Volkov, Sergey I Bozhevolnyi, Eloïse Devaux, Jean-Yves Laluet, and Thomas W Ebbesen. Wavelength selective nanophotonic components utilizing channel plasmon polaritons. *Nano letters*, 7(4):880–884, 2007.

[46] Wenjun Wu, Junbo Yang, Jingjing Zhang, Jie Huang, Dingbo Chen, and Hongqing Wang. Ultra-high resolution filter and optical field modulator based on a surface plasmon polariton. *Optics Letters*, 41(10):2310–2313, 2016.

[47] Vladimir A Zenin, Valentyn S Volkov, Zhanghua Han, Sergey I Bozhevolnyi, Eloïse Devaux, and Thomas W Ebbesen. Directional coupling in channel plasmon-polariton waveguides. *Optics Express*, 20(6):6124–6134, 2012.

[48] Donald M Mattox. *Handbook of physical vapor deposition (PVD) processing*. William Andrew, 2010.

[49] Milton Ohring. *Materials science of thin films: depositon & structure*. Elsevier, 2001.

[50] Richard C Jaeger. *Introduction to microelectronic fabrication*. Addison-Wesley Longman Publishing Co., Inc., 1987.

[51] Daniel Berkoh and Sarang Kulkarni. Challenges in lift-off process using camp negative photoresist in iii–v ic fabrication. *IEEE Transactions on Semiconductor Manufacturing*, 32(4):513–517, 2019.

[52] Richard W Johnson, Adam Hultqvist, and Stacey F Bent. A brief review of atomic layer deposition: from fundamentals to applications. *Materials today*, 17(5):236–246, 2014.

[53] Mikko Ritala, Kaupo Kukli, Antti Rahtu, Petri I Raisanen, Markku Leskela, Timo Sajavaara, and Juhani Keinonen. Atomic layer deposition of oxide thin films with metal alkoxides as oxygen sources. *Science*, 288(5464):319–321, 2000.

[54] Shibnath Pathak. Photonics integrated circuits. In *Nanoelectronics*, pages 219–270. Elsevier, 2019.

[55] P Berini, R Charbonneau, N Lahoud, and G Mattiussi. Characterization of long-range surface-plasmon-polariton waveguides. *Journal of Applied Physics*, 98(4):043109, 2005.

[56] Jan Kischkat, Sven Peters, Bernd Gruska, Mykhaylo Semtsiv, Mikaela Chashnikova, Matthias Klinkmüller, Oliana Fedosenko, Stephan Machulik, Anna Aleksandrova, Gregorii Monastyrskyi, et al. Mid-infrared optical properties of thin films of aluminum oxide, titanium dioxide, silicon dioxide, aluminum nitride, and silicon nitride. *Applied optics*, 51(28):6789–6798, 2012.

[57] Martin M Frank, Steven J Koester, Matthew Copel, John A Ott, Vamsi K Paruchuri, Huiling Shang, and Rainer Loesing. Hafnium oxide gate dielectrics on sulfur-passivated germanium. *Applied physics letters*, 89(11):112905, 2006.

[58] Jin Won Seo, Ch Dieker, J-P Locquet, G Mavrou, and A Dimoulas. Hf o 2 high-k dielectrics grown on (100) ge with ultrathin passivation layers: Structure and interfacial stability. *Applied Physics Letters*, 87(22):221906, 2005.

[59] Hyoungsub Kim, Paul C McIntyre, Chi On Chui, Krishna C Saraswat, and Mann-Ho Cho. Interfacial characteristics of hf o 2 grown on nitrided ge (100) substrates by atomic-layer deposition. *Applied physics letters*, 85(14):2902–2904, 2004.

[60] EP Gusev, Huiling Shang, Matt Copel, M Gribelyuk, C D'emic, P Kozlowski, and T Zabel. Microstructure and thermal stability of hfo 2 gate dielectric deposited on ge (100). *Applied physics letters*, 85(12):2334–2336, 2004.

[61] Bart Onsia, Thierry Conard, Stefan De Gendt, Marc Heyns, Ilse Hoflijk, Paul Mertens, Marc Meuris, G Raskin, Sonja Sioncke, Ivo Teerlinck, et al. A study of the influence of typical wet chemical treatments on the germanium wafer surface. *Solid State Phenomena*, 103(104):27–30, 2005.

[62] Qi Xie, Shaoren Deng, Marc Schaekers, Dennis Lin, Matty Caymax, Annelies Delabie, Xin-Ping Qu, Yu-Long Jiang, Davy Deduytsche, and Christophe Detavernier. Germanium surface passivation and atomic layer deposition of high-k dielectrics—a tutorial review on ge-based mos capacitors. *Semiconductor Science and Technology*, 27(7):074012, 2012.

[63] Chi On Chui, Hyoungsub Kim, Paul C McIntyre, and Krishna C Saraswat. Atomic layer deposition of high-/spl kappa/dielectric for germanium mos applications-substrate. *IEEE Electron Device Letters*, 25(5):274–276, 2004.

[64] P Ponath, AB Posadas, and AA Demkov. Ge (001) surface cleaning methods for device integration. *Applied Physics Reviews*, 4(2):021308, 2017.

[65] Dennis M Hausmann, Esther Kim, Jill Becker, and Roy G Gordon. Atomic layer deposition of hafnium and zirconium oxides using metal amide precursors. *Chemistry of materials*, 14(10):4350–4358, 2002.

[66] Robert G Hunsperger and Jurgen R Meyer-Arendt. Integrated optics: theory and technology. *Applied Optics*, 31(3):298, 1992.

[67] Jin Tae Kim, Suntak Park, Jung Jin Ju, Seung Koo Park, Min-Su Kim, and Myung-Hyun Lee. Low-loss polymer-based long-range surface plasmon-polariton waveguide. *IEEE Photonics Technology Letters*, 19(18):1374–1376, 2007.

[68] N Kinsey, M Ferrera, VM Shalaev, and A Boltasseva. Examining nanophotonics for integrated hybrid systems: a review of plasmonic interconnects and modulators using traditional and alternative materials. *JOSA B*, 32(1):121–142, 2015.

[69] Richard Soref, Joshua Hendrickson, and Justin W Cleary. Mid-to long-wavelength infrared plasmonic-photonics using heavily doped n-ge/ge and n-gesn/gesn heterostructures. *Optics express*, 20(4):3814–3824, 2012.

[70] Justin W Cleary, William H Streyer, Nima Nader, Shiva Vangala, Ivan Avrutsky, Bruce Claflin, Joshua Hendrickson, Daniel Wasserman, Robert E Peale, Walter Buchwald, et al. Platinum germanides for mid-and long-wave infrared plasmonics. *Optics express*, 23(3):3316–3326, 2015.

[71] Richard Soref, Robert E Peale, and Walter Buchwald. Longwave plasmonics on doped silicon and silicides. *Optics express*, 16(9):6507–6514, 2008.

[72] PD Ye, GD Wilk, J Kwo, BAYB Yang, H-JL Gossmann, MAFM Frei, SNG Chu, JP Mannaerts, MASM Sergent, MAHM Hong, et al. Gaas mosfet with oxide gate dielectric grown by atomic layer deposition. *IEEE Electron Device Letters*, 24(4):209–211, 2003.

[73] K Lisa, Jeffrey Travis, Crystal Rolfson, and David Weber. Labview for everyone: graphical programming made even easier. 1997.